2013

Gravitational Waves From Perturbed Kerr Black Holes: Two Investigations

Zhongyang Zhang
University of Mississippi

GRAVITATIONAL WAVES FROM PERTURBED KERR BLACK HOLES: TWO INVESTIGATIONS

A Thesis
presented in partial fulfillment of requirements
for the degree of Master of Science
in the Department of Physics and Astronomy
The University of Mississippi

by

ZHONGYANG ZHANG

August 2014

ABSTRACT

This thesis includes two main projects. The first project is a study of the effect of black hole spin on the accuracy of the post-Newtonian approximation. We focus on the gravitational energy produced by the quasicircular, equatorial, extreme mass-ratio inspiral of a compact object into a Kerr black hole of mass M and spin J. For a given dimensionless spin $a \equiv J/M^2$ (in geometrical units $G = c = 1$), the energy flux depends only on the orbital velocity v or (equivalently) on the Boyer-Lindquist orbital radius r. We investigate the formal region of validity of the Taylor post-Newtonian expansion of the energy flux (which is known up to order v^8 beyond the quadrupole formula) by comparing the expansion to numerical calculations of the flux. We find that, at any fixed post-Newtonian order, the edge of the region of validity (as measured by $v/v_{\rm ISCO}$, where $v_{\rm ISCO}$ is the orbital velocity at the innermost stable circular orbit) is only weakly dependent on a. Independently of a, the inclusion of angular multipoles up to and including $\ell = 5$ in the numerical flux is necessary to achieve the level of accuracy of the best-known (v^8) expansion of the energy flux.

In the second project we study the excitation of Kerr black holes produced by infalling particles. Such a study requires an accurate knowledge of the Green's function describing the response of the black hole to external perturbations. Relying on the formalism developed by Mano, Suzuki and Takasugi, we improve and extend previous calculations of the contribution to the Green's function coming from quasinormal mode residues in the complex frequency plane ("excitation factors B_q"). Using these results we compute the "excitation coefficients" C_q (the mode amplitudes) when the source of the perturbations is a particle falling into the black hole along the symmetry axis. We compare this calculation with numerical integrations of the perturbation equations, and we show quantitatively how the addition of higher overtones improves the agreement with the numerical waveforms.

DEDICATION

This thesis is dedicated to everyone who helped me and guided me.

ACKNOWLEDGEMENTS

It was a great fortune for me to have Dr. Berti as my thesis advisor in the past three years. I thank him for his great patience and advice in guiding and helping me. I am grateful to Dr. Bombelli, Dr. Datta, Dr. Raspet and Dr. Gladden, who gave me a lot of help in my academic studies at Ole Miss. I gratefully thank Dr. Chen for his great help and advice in guiding me when I visited Caltech. I am grateful to Dr. Yunes and Dr. Cardoso, who gave me a lot of help to finish the papers, and to my friends Chen Liang, Tian Yun and Gao Caixia for their help. Finally, I greatly thank my parents for their help and support.

TABLE OF CONTENTS

LIST OF FIGURES

LIST OF TABLES

CHAPTER 1

INTRODUCTION

This thesis studies the gravitational radiation produced by particles around a rotating (Kerr) black hole. The first part of the thesis studies the radiation emitted by particles in circular, equatorial orbits around the black hole by comparing a post-Newtonian expansion of the energy flux to numerical calculations. The second part of the thesis studies the excitation of the characteristic oscillation modes of the black hole ("quasinormal modes") by particles falling into the hole along the rotation axis. In this introduction we present a short summary of these two research projects.

The post-Newtonian approximation for particles in circular, equatorial orbits around Kerr black holes

Binaries of compact objects, such as black holes (BHs) and/or neutron stars, are one of the main targets for gravitational-wave (GW) observations. When the binary members are widely separated, their slow inspiral can be well-described by the post-Newtonian (PN) approximation, a perturbative *asymptotic* expansion of the "true" solution of the Einstein equations. The small expansion parameter in the PN approximation is v/c, where v is the orbital velocity of the binary and c is the speed of light. Asymptotic expansions, however, must be used with care, as the inclusion of higher-order terms does not necessarily lead to an increase in accuracy. Therefore one would like to determine the optimal order of expansion and the formal region of validity of the PN asymptotic series [3, 50], i.e., the order and region inside which the addition of higher order terms increases the accuracy of the approximation in a convergent fashion.

The accuracy of the PN approximation for quasicircular, nonspinning (Schwarzschild), extreme mass-ratio inspirals (EMRIs) case was investigated by Yunes and Berti in Ref. [50]. By comparing the PN expansion of the energy flux to numerical calculations in the perturbative Teukolsky formalism, Yunes and Berti concluded that (i) the region of validity of the PN expansion is largest at relative 3PN order – i.e., order $(v/c)^6$ (throughout this paper, a term of $\mathcal{O}(v^{2N})$ is said to be of NPN order); and (ii) the inclusion of higher multipoles in numerical calculations is necessary to improve the agreement with PN expansions at large orbital velocities. The fact that the region of validity is largest at 3PN could be a hint that the series actually *diverges* beyond 3PN order, at least in the extreme mass-ratio limit.

In chapter 2, we extend that study to EMRIs for which the more massive component is a *rotating* (Kerr) BH. The present analysis focuses on the effect of the BH spin on the accuracy of the PN expansion. We generalize the methods presented in Ref. [50] to take into account certain pathological behaviors of the *error function*, used to determine the region of validity. This generalization may also be applicable to comparable-mass systems.

A surprising result we find is that the edge of the region of validity (the maximum velocity beyond which higher-order terms in the series cannot be neglected), normalized to the velocity at the innermost stable circular orbit, is weakly dependent on the dimensionless Kerr spin parameter a. In fact, this edge is roughly in the range $v/v_{\rm ISCO} \in [0.3, 0.6]$ for almost all PN orders, irrespective of a. This suggests, perhaps, that the ratio $v/v_{\rm ISCO}$ is a better PN expansion parameter than v/c, when considering spinning BHs.

Another surprising result is related to the behavior of the edge of the region of validity as a function of PN order. In the nonspinning case, beyond 3PN order, $\mathcal{O}(v^6/c^6)$, this edge seemed to consistently decrease with PN order [50]. This was studied up to $\mathcal{O}(v^{11}/c^{11})$, the largest PN order known for the nonspinning case. In the spinning case, however, the series is known only up to $\mathcal{O}(v^8/c^8)$, and we are thus unable to conclusively determine if the trend found in the nonspinning case persists. Higher-order calculations will be necessary to draw more definite conclusions.

Numerical (or in this case, perturbative) calculations of the energy flux rely on multipolar decompositions of the angular dependence of the radiation. By comparing the convergence of the multipolar decomposition to the convergence of the PN expansion of the energy flux, we find that for $v/c \sim 0.1$ the inclusion of multipoles up to and including $\ell = 5$ seems necessary to achieve the level of accuracy of the best-known ($N = 8$) PN expansion of the flux. These conclusions are also largely independent of the spin parameter a.

Quasinormal mode excitation of Kerr black holes

Distorted black holes (BHs) emit gravitational radiation. A spectral decomposition of the perturbation response of the Schwarzschild [25] and Kerr [9] geometries using Green's function techniques shows that a discrete sum of QNMs – damped oscillations whose frequencies and damping times depend only on the BH mass and angular momentum – will dominate the response at all but very early and very late times. Because of the qualitative similarity with a ringing bell, this intermediate stage is known as "ringdown" in the gravitational-wave literature [42, 34, 12].

Numerical simulations show that binary BH mergers in general relativity inevitably result in the formation of a distorted rotating remnant, which radiates ringdown waves while settling down into a stationary (Kerr) solution of the Einstein equations in vacuum. Despite the great advances in binary BH simulations in four [27, 67, 36] and higher dimensions [66], the excitation of the QNMs of the remnant BH resulting from a merger is still poorly understood. Perturbative techniques are especially valuable to understand ringdown excitation in situations that pose a particular challenge to numerical simulations, namely:

1) *Large mass-ratio binaries.* One of the frontiers in numerical simulations of BH mergers are quasicircular binaries with large mass ratios. Progress in this direction has been slow but steady, both in the quasicircular case – where initial record mass ratios $q = m_1/m_2 = 10$ [40] have been broken using "hybrid" techniques [5, 33] – and in the head-on case, where simulations with $q = 100$ have recently been performed using different approaches [68, 75]. In

this regime, perturbation theory is crucial to validate and/or optimize numerical simulations.
2) *Large spins.* Numerical simulations of BH binaries are usually carried out using either the Baumgarte-Shapiro-Sasaki-Nakamura (BSSN) formulation of the Einstein equations and a finite-difference scheme, or using the harmonic formulation and spectral methods. The first class of simulations is limited to dimensionless spins $a/M = J/M^2 \lesssim 0.93$, because this is the maximum spin that can be achieved with puncture initial data [6]. Initial data with spins as large as $a/M \sim 0.97$ can be constructed [30] and have been evolved using spectral codes [29, 28]. These simulations present a significant challenge for modeling efforts using effective-one-body techniques when one considers binaries with aligned spins $a/M \gtrsim 0.7$ [2]. Models of the late merger and ringdown phase can be significantly improved by using first-principle calculations in BH perturbation theory, rather than a phenomenological matching of inspiral waveforms with QNM superpositions of largely arbitrary amplitudes and starting times.
3) *Higher dimensions.* Numerical simulations in higher dimensions are very challenging, and simple calculations in BH perturbation theory can give insight into the results of the simulations. For example, the qualitative behavior of the energy and linear momentum radiated by particles falling into higher-dimensional Schwarzschild-Tangherlini BHs (predicted in Refs. [10, 13]) is in excellent agreement with the first numerical simulations in $D = 5$ [38]: see, e.g., Refs. [32, 73] for reviews.

First-principle calculations of QNM excitation in four space-time dimensions would be particularly beneficial in building semianalytical models of the merger/ringdown phase, to be used as matched-filtering templates in gravitational-wave searches. In chapter 3, we carry out these calculations in four spacetime dimensions considering, for simplicity, head-on particle infalls into Schwarzschild and Kerr BHs. Our study improves and exs the results of Ref. [9].

CHAPTER 2

ACCURACY OF THE POST-NEWTONIAN APPROXIMATION

This chapter is organized as follows. In Section 2.1 we present the energy flux radiated by quasicircular, equatorial Kerr EMRIs in the adiabatic approximation, as computed in PN theory [23, 37, 65] and with accurate frequency-domain codes in BH perturbation theory [47, 48, 49]. In Section 2.2 we discuss the region of validity of the PN approximation in terms of the normalized orbital velocity $v/v_{\rm ISCO}$ and of the normalized orbital radius $r/r_{\rm ISCO}$, where the "ISCO" subscript stands for "innermost stable circular orbit". We consider both corotating and counterrotating orbits. In Section 2.3 we study the number of multipolar components that must be included in the *numerical* flux in order to achieve sufficient accuracy. Finally, in Section 4 we present our conclusions. We follow the same notation as in Ref. [50] and we use geometrical units ($G = c = 1$).

2.1 Energy flux for quasicircular, equatorial EMRIs in Kerr: numerical and PN results

In the PN approximation, the GW energy flux radiated to infinity by a test particle in a circular orbit and on the equatorial plane of a Kerr BH is given by [37, 65, 23]

$$F^{(N)} = F_{\rm Newt}\left[\sum_{k=0}^{N}(a_k + b_k\,\ln v)\,v^k\right]\,. \tag{2.1}$$

This flux is known up to $N = 8$ when including spins, and up to $N = 11$ in the nonspinning case. The leading (Newtonian) contribution[1] is

$$F_{\rm Newt} = \frac{32}{5}\frac{\mu^2}{M^2}v^{10}\,, \tag{2.2}$$

[1]Notice that there is a typo in Eq. (18) of Ref. [50].

where μ and M are the test particle mass and Kerr BH mass, respectively. As we are here interested in the accuracy of the PN approximation, we will ignore the flux of energy going into the horizon, which cannot always be neglected when building waveform templates.

The expansion coefficients a_k and b_k contain both spin-independent and spin-dependent terms, where the dimensionless spin parameter a is related to the Kerr BH spin angular momentum via $J = aM^2$. These coefficients can be found in Eq. (G19) of Ref. [37], so we do not list them explicitly[2]. Note that logarithmic terms only appear at 3PN and 4PN (i.e., $b_6 \neq 0$ and $b_8 \neq 0$), and that the (a_k, b_k) for $8 < k \leq 11$ are known *only* in the spin-independent limit.

We will denote by v the orbital velocity, defined as $v \equiv (M\Omega)^{1/3}$ (where Ω is the small body's orbital frequency), and related to the Boyer-Lindquist radius r by

$$\frac{r}{M} = \frac{(1 - av^3)^{2/3}}{v^2} \,, \tag{2.3}$$

whose inverse is

$$v = \left[(r/M)^{3/2} + a\right]^{-1/3} \,. \tag{2.4}$$

At the ISCO we have [41]

$$\frac{r_{\rm ISCO}}{M} = 3 + Z_2 - \sqrt{(3 - Z_1)(3 + Z_1 + 2Z_2)} \,, \tag{2.5}$$

$$Z_1 \equiv 1 + (1 - a^2)^{1/3} \left[(1 + a)^{1/3} + (1 - a)^{1/3}\right] \,,$$

$$Z_2 \equiv (3a^2 + Z_1^2)^{1/2} \,, \tag{2.6}$$

where $a > 0$ ($a < 0$) corresponds to corotating (counterrotating) orbits.

[2] See also their Eq. (3.40), that provides a similar expansion in terms of the PN orbital velocity parameter $v' = \sqrt{M/r_0}$.

Using Eqs. (2.3) and (2.5), we also have

$$\frac{r}{r_{\rm ISCO}} = \frac{(1-av^3)^{2/3}}{v^2\left[3+Z_2 \mp \sqrt{(3-Z_1)(3+Z_1+2Z_2)}\right]}\,.$$

The ISCO velocity can be found by replacing $r_{\rm ISCO}$ in Eq. (2.5) into the velocity-radius relation (2.4). The velocity $v_{\rm ISCO}$ and the radius $r_{\rm ISCO}/M$ are displayed graphically in Fig. 2.1. Observe that, although $r_{\rm ISCO} \to M$ as $a \to 1$, $v_{\rm ISCO}$ is bounded by $2^{-1/3} \simeq 0.79$.

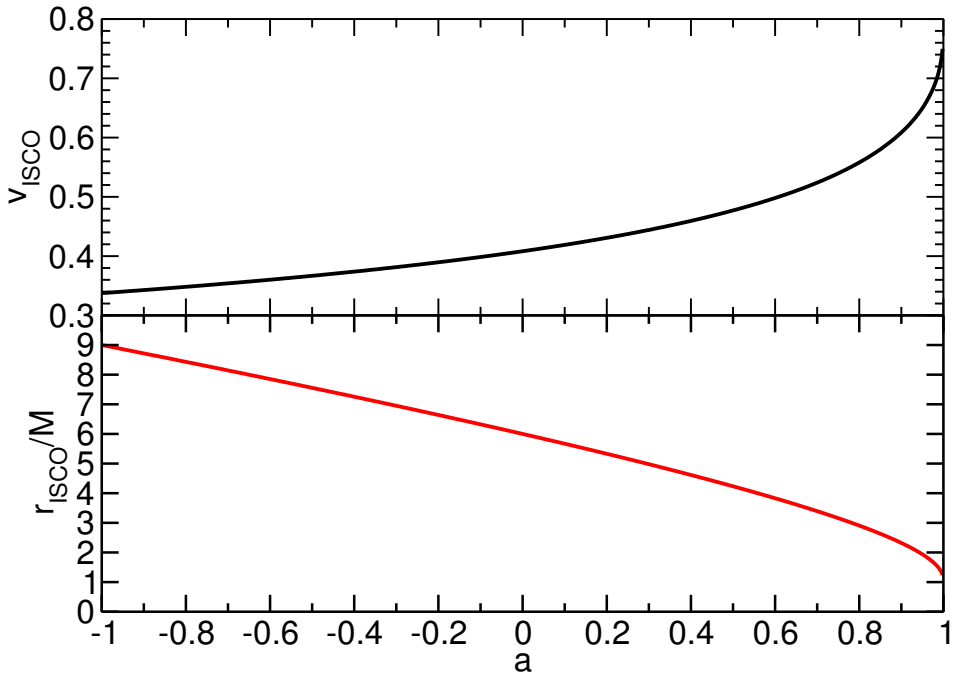

Figure 2.1

ISCO velocity ($v_{\rm ISCO}$, top panel) and radius ($r_{\rm ISCO}/M$, bottom panel) as a function of a. Here and elsewhere we use the convention that a negative spin parameter refers to counterrotating orbits.

The rigorous definition of velocity is a tricky business in general relativity. We have here chosen to define velocity in a quasi-Newtonian fashion, in terms of the angular velocity and Kepler's law. One can think of this velocity as that which would be measured by an observer at spatial infinity. On the other hand, one can also study the velocity measured by an observer in the neighborhood of the BH and that is rotating with the geometry; this

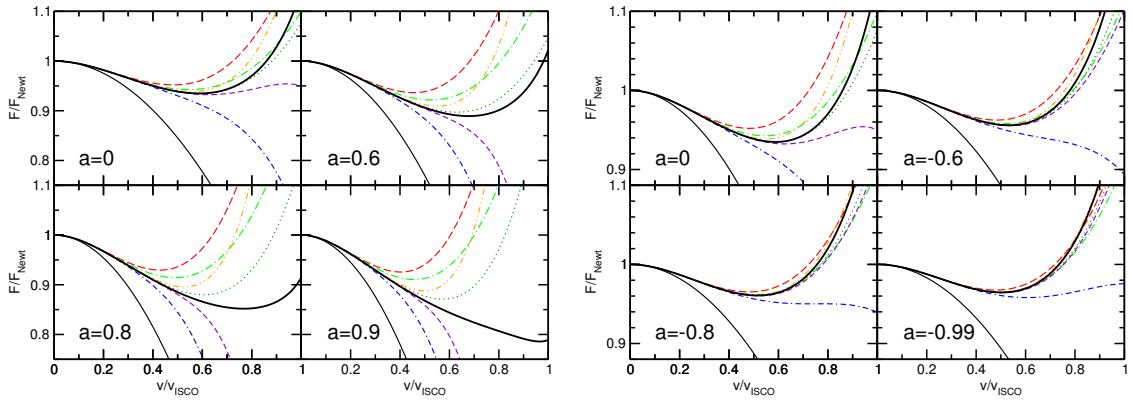

Figure 2.2

Gravitational energy flux (normalized to $F_{\rm Newt}$) as a function of the normalized orbital velocity, $v/v_{\rm ISCO}$. The left panel is for corotating orbits, and the right panel for counterrotating orbits. Different insets refer to different spin parameters a, as indicated. The thick black line is the numerical flux. Other linestyles refer to different PN approximations: $F^{(2)}$ (thin black), $F^{(3)}$ (long-dashed red), $F^{(4)}$ (dash-dotted green), $F^{(5)}$ (dash-dash-dotted blue), $F^{(6)}$ (dash-dot-dotted orange), $F^{(7)}$ (dotted dark green), $F^{(8)}$ (short-dashed violet).

quantity would differ from v in Eq. (2.4), and, in fact, its associated $v_{\rm ISCO}$ would tend to $1/2$ in the limit $a \to 1$ (see, e.g., Eq. (3.11b) in Ref. [41]). This shows that the $a \to 1$ limit is very delicate, and the precise value of the velocity field is an observer-dependent (and non-invariant) quantity. However, once a definition is chosen, the velocity is a perfectly good quantity to parametrize the structure of the PN series.

A first guess at the asymptotic behavior of this series can be obtained by simply plotting different PN approximants $F^{(N)}$ and comparing them with high-accuracy, numerical results for the energy flux, obtained from a frequency-domain Teukolsky code (see Refs. [23, 77] for early work in the Schwarzschild case, and Fig. 9 in Ref. [78] for a related discussion in the Kerr context). The numerical results used in this comparison are the same as those used in Refs. [47, 48, 49] to study the accuracy of a resummed effective-one-body version of the PN approximation to model EMRIs. They consist of numerical fluxes, evaluated for spin parameters ranging from $a = 0$ to $a = 0.9$ in steps of $\Delta a = 0.1$ (in fact, we also have access to the counterrotating flux for $a = -0.99$). The typical accuracy of these fluxes is better than one part in 10^{10} for all velocities and spins. We refer the reader to Section IIB

of Ref. [49] for a more detailed description of the code.

Figure 2.2 compares the different PN approximations to the numerical flux. The left panel refers to corotating orbits, and the right panel to counterrotating orbits. Different insets correspond to different values of the BH spin, and different linestyles represent different orders in the PN expansion. As stated earlier, in this figure and in the rest of this paper, we neglect energy absorption by the BH. Observe that, as first noted by Poisson in the Schwarzschild case [23], the behavior of the PN expansion is quite erratic. For any given a, rather than converging monotonically, higher-order approximations keep undershooting and overshooting with respect to the "exact" numerical result. This oscillatory behavior is quite typical of asymptotic expansions, and it has been studied in depth, especially for extreme mass-ratio inspirals into nonrotating BHs [23, 77]. Various authors proposed different schemes to accelerate the convergence of the PN expansion, including Padé resummations [62, 63, 1] and the use of Chebyshev polynomials [20]. The asymptotic properties of these resummation techniques are an interesting topic for future study.

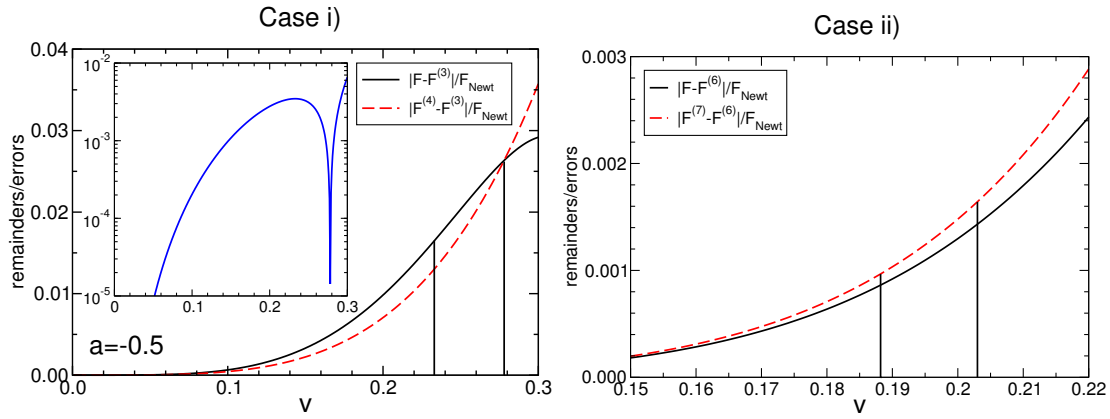

Figure 2.3

Left: absolute value of the remainder of the $N = 3$ PN flux, $|F - F^{(3)}|/F_{\rm Newt}$ (solid line), and the $N = 4$ term $|F^{(4)} - F^{(3)}|/F_{\rm Newt}$ (dashed red line). The inset shows the modulus of their difference, Eq. (2.8), in a semilogarithmic scale. Right: same as the left panel, but for the $N = 6$ remainder and $N = 7$ term. All curves in this plot refer to the counterrotating case with spin $a = -0.5$. The lower (v_l, more conservative) and upper ($\bar{v}$, less conservative) edges of the region of validity are (somewhat conventionally) delimited by the vertical lines, as explained in the main text.

This figure provides some clues about the edge of the region of validity of the PN approximation. For corotating orbits (left panel of Fig. 2.2), as the spin increases from zero to $a = 0.9$, the higher-order PN approximants start to deviate from numerical results at lower values of $v/v_{\rm ISCO}$: this happens roughly when $v/v_{\rm ISCO} \simeq 0.6$ for $a = 0$, and when $v/v_{\rm ISCO} \simeq 0.4$ for $a = 0.9$. This leads us to naively expect a shrinking of the region of validity of the PN approximation as a function of positive a. This expectation will be validated (at least qualitatively) in Section 2.2: cf. the bottom-right panel of Fig. 2.4 below.

At first sight, the results for counterrotating orbits (right panel of Fig. 2.2) seem surprisingly good. In particular, the 3PN approximation (dash-dot-dotted, orange line) is almost indistinguishable from the numerical result all the way up to $v = v_{\rm ISCO}$ when the spin is large. Such a good performance is simply because of the well-known, monotonically-increasing behavior of $v_{\rm ISCO}$ with spin, with a minimum as $a \to -1$ (cf. Fig. 2.1). Since counterrotating orbits probe a smaller range in v/c (up to $v/c \sim 0.35$ for fast-spinning BHs), the PN approximation is more accurate. Unfortunately, prograde accretion is likely to be more common than retrograde accretion in astrophysical settings (see, e.g., Ref. [11]). Moreover, the 3.5PN and 4PN approximants are significantly *worse* than the 3PN one at $a = -0.99$. This is consistent with the PN series being an asymptotic expansion, as one of the characteristic features of the latter is that beyond a certain optimal order, higher-order approximants become less accurate [3].

2.2 Region of validity

Let us now turn to determining the region of validity of the PN approximation for different values of the BH spin. For a complete review of asymptotic approximation techniques we refer the reader to Ref. [3]. Ref. [50] presents a short introduction to the topic in the present context. As explained in those references, the edge of the region of validity is

determined by the approximate condition

$$\mathcal{O}(F - F^{(N)}) = \mathcal{O}(F^{(N+1)} - F^{(N)})\,, \tag{2.7}$$

where F denotes the "true" (numerical) result for the GW energy flux and $F^{(N)}$ denotes the N-th order PN approximation.

An inherent and *intrinsic* ambiguity is contained in Eq. (2.7), encoded in the order symbol. This makes *any* definition of the region of validity of an asymptotic series somewhat imprecise. As shown in Fig. 2.3 (or in Fig. 8 of Ref. [50]), there are two qualitatively different scenarios:

i) Left panel of Fig. 2.3: The next-order term $|F^{(N+1)} - F^{(N)}|$ starts off smaller than the remainder $|F - F^{(N)}|$, but eventually they cross and separate. We can then estimate the edge of the region of validity $\bar{v}$ by solving $\delta^{(N)}(\bar{v}) = 0$, where

$$\delta^{(N)}(v) \equiv \big||F - F^{(N)}| - |F^{(N+1)} - F^{(N)}|\big| \tag{2.8}$$

is the *error function*. If we also define a more conservative *lower edge* of the region of validity, v_l, as the point where

$$\left.\frac{d\delta^{(N)}(v)}{dv}\right|_{v_l} = 0\,, \tag{2.9}$$

we can then introduce an *uncertainty width* of the region of validity: $\delta\bar{v} \equiv \bar{v} - v_l$; see the inset of the left panel of Fig. 2.3.

ii) Right panel of Fig. 2.3: The remainder and the next-order term are of the same order for sufficiently low velocities, until eventually the curves separate for larger velocities. This situation is the rule, rather than the exception, for the problem we consider in this paper. When this happens, method i) cannot be applied, because $\delta^{(N)}(v) = 0$ has

no solutions. Given the approximate nature of the order relationship in Eq. (2.7), we can *define* the region of validity as the point $\bar{v}$ such that $\delta^{(N)}(\bar{v}) = \delta_0$, where δ_0 is some given tolerance defined below.

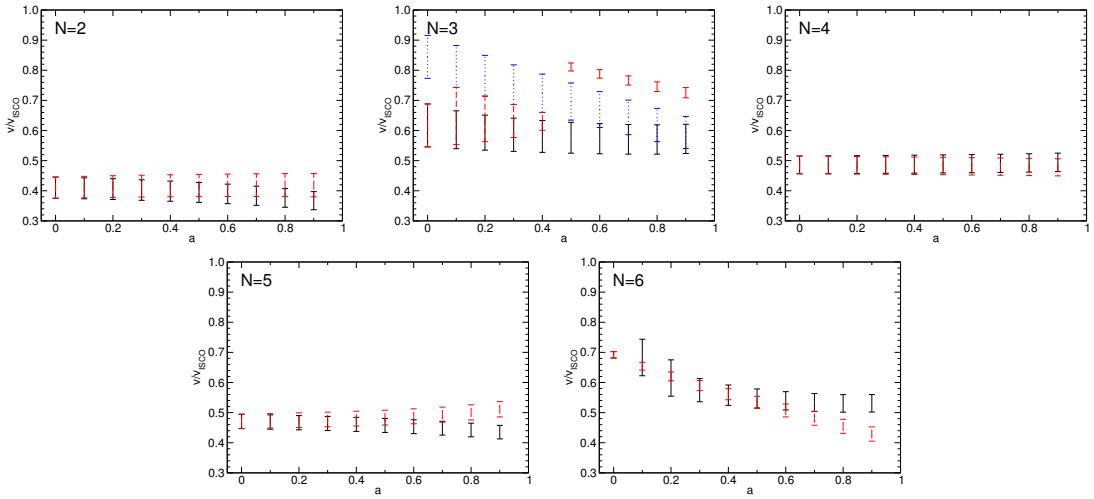

Figure 2.4

Edge of the region of validity as a function of a for different PN orders, in the corotating (black, straight line) and counterrotating (red, dashed line) cases. The blue, dashed lines for $N = 3$ refer to the counterrotating case, and they were obtained by an alternative method (see the discussion around Fig. 2.7 below).

Higher-order approximations should be sensitive to a smaller tolerance, which implies that δ_0 cannot be set arbitrarily. Instead, δ_0 should be given by the error in the difference between the Nth remainder and the $(N+1)$th-order term. This error is presumably of the order of the error in the $(N+1)$th-order term, and it can be estimated by the $(N+2)$th-order term. The imprecision of the order symbol is now encoded in the fact that δ_0 depends on v. We can try to estimate its value by evaluating the $(N+2)$th order term in the middle of the allowed range, that is, at $v_{\rm ISCO}/2$:

$$\delta_0 = \left| F^{(N+2)}(v_{\rm ISCO}/2) - F^{(N+1)}(v_{\rm ISCO}/2) \right| . \tag{2.10}$$

This estimate of δ_0 is not exact, so we can try to provide a more conservative lower edge of

the region of validity, v_l, by imposing the condition[3] $\delta^{(N)}(v_l) = \delta_0/2$. We can then define an uncertainty on the region of validity $\delta\bar{v} = |\bar{v} - v_l|$. This is illustrated pictorially by the vertical lines in the right panel of Fig. 2.3.

Let us now discuss the behavior of the edge of the region of validity as a function of the PN order N and of the BH spin a. The corotating and counterrotating regions of validity and the associated errors are shown in Fig. 2.4 with solid black (dashed red) error bars for corotating (counterrotating) orbits, respectively.

Let us first consider the corotating case (solid black error bars). All results were obtained using method ii) above. At any fixed PN order, the normalized region of validity $v/v_{\rm ISCO}$ remains roughly constant as a function of a. With a few exceptions, the most conservative estimate v_l (lower edge of the error bars in the plots) is typically in the range $v/v_{\rm ISCO} \in [0.3\,, 0.6]$. This is consistent with the left panel of Fig. 2.2, where we see that all PN approximations (including high-order ones) peel off from the numerical flux in this range.

These figures allow us to arrive at an interesting conclusion. When we recall that $v_{\rm ISCO}$ increases with a (cf. Fig. 2.1), the figures suggest that spin-dependent corrections in the PN expansion of Eq. (2.1) are effective at pushing the validity of the PN expansion to higher values of v/c. However, there is an intrinsic limit to what is achievable, which is determined instead by $v/v_{\rm ISCO}$, and roughly independent of a. In the range $a \in [0.3\,, 0.9]$, $v_{\rm ISCO}$ increases from $\simeq 0.444$ to $\simeq 0.609$. Therefore the region of validity for the orbital velocity is approximately in the range $v/c \in [0.44 \times 0.3\,, 0.61 \times 0.6] \sim [0.13\,, 0.37]$.

Let us now focus on the counterrotating case, i.e., on the dashed red error bars in Fig. 2.4, which, again, were determined using method ii) above. The only exception is the case $N = 3$ (corresponding to the right panel of Fig. 2.3), that we will discuss separately below. As in the corotating case, the region of validity shrinks mildly or remains roughly constant as $|a|$ increases. For $N = 6$ the region of validity shrinks faster with increasing spin.

[3]Note that in the Erratum of Ref. [50] we impose a slightly different condition: $\delta(v_l) = \delta_0/2$, $\delta(\bar{v}) = 2\delta_0$.

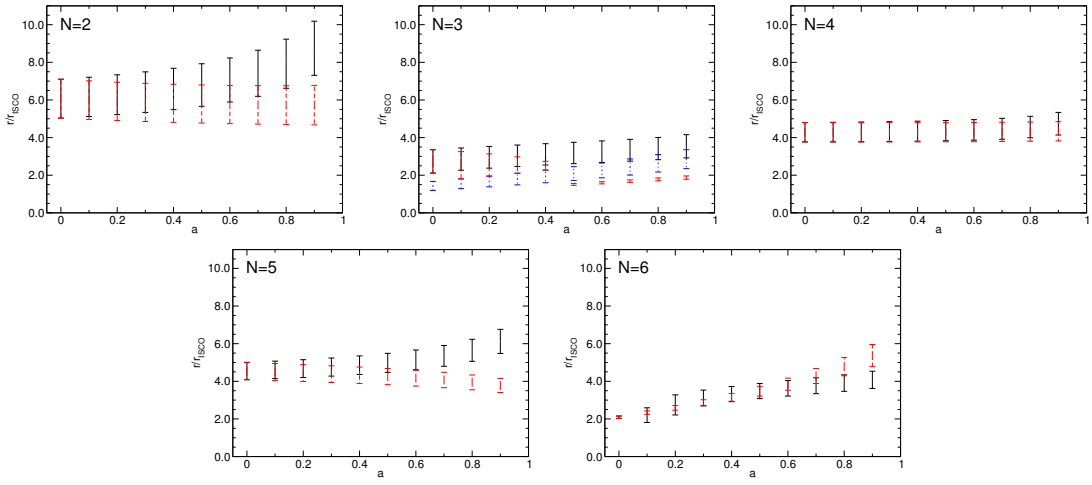

Figure 2.5

Edge of the region of validity expressed in terms of the Boyer-Lindquist radius for different PN orders, in the corotating (black, straight line) and counterrotating (red, dashed line) cases. The blue, dashed lines for $N = 3$ refer to the counterrotating case, and they were obtained by an alternative method (see the discussion around Fig. 2.7 below).

The edge of the region of validity can also be presented in terms of the Boyer-Lindquist radius of the particle's circular orbit. The corresponding plots for the corotating and counterrotating cases are presented, for completeness, in Fig. 2.5. The ISCO radius $r_{\rm ISCO}$ is a monotonically decreasing function of the spin (or of $v_{\rm ISCO}$), so, quite naturally, the trend as a function of a is the opposite of what we observed for velocities in Fig. 2.4. Our results consistently suggest that the region of validity of the PN approximation cannot be extended all the way down to the ISCO, contrary to a rather common assumption in GW data analysis. Instead, one should use care when using, for example, the 2PN approximation for $r/r_{\rm ISCO} < 4$, as in that regime higher-order PN terms cannot be neglected (this is particularly true for rapidly rotating BHs in prograde orbits). Our results suggest that a safer choice would be to truncate all analyses at $r/r_{\rm ISCO} = 6$, which ranges between $r/M \in [6\,,54]$ depending on the BH spin, unless one is dealing with approximants more accurate than Taylor expansions.

Finally, one can also investigate how the edge of the region of validity behaves with PN order. This is depicted in Fig. 2.6 for a set of fixed values of a (shown with different colors,

as described in the caption). The vertical dashed lines separate the different-N orders. If we concentrate on the nonspinning case (black), ignore the pathological case $N = 3$ (discussed below) and consider the conservative, lower end of the error bar, we see that there is a maximum at $N = 6$. For larger values of N, $v/v_{\rm ISCO}$ would consistently decrease, as found in Ref. [50]. In the spinning case, however, this trend is not as clear, as at $N = 6$ the edge of the region of validity is rather sensitive to the spin value. Without higher-order terms in the PN expansion, which would provide larger-N points in this figure, one cannot conclude whether $N = 6$ is the optimal order of expansion in the spinning case.

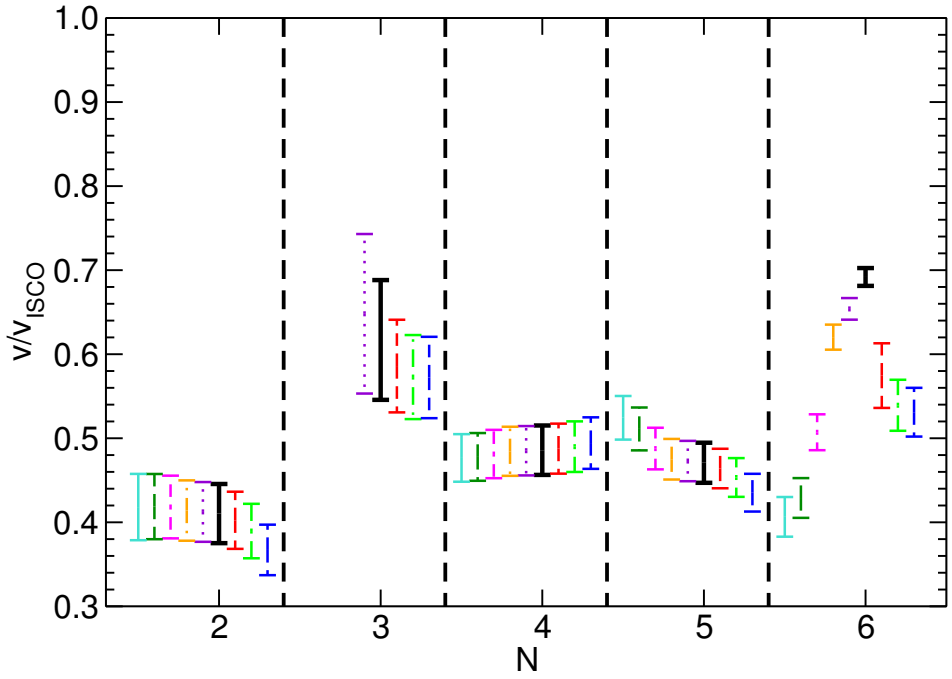

Figure 2.6

Edge of the region of validity as a function of N for fixed values of a. The thick, black error bar corresponds to $a = 0$, followed by $a = 0.3\,, 0.6\,, 0.9$ to the right and $a = -0.1\,, -0.2\,, -0.6\,, -0.9\,, -0.99$ to the left. Note that $N = 3$ is a special case. For reasons discussed in the text, we do not give error bars for $N = 3$ and $a < -0.1$.

Before moving on to the next Section, let us discuss the $N = 3$ case for counterrotating orbits in more detail. This is a special case, as noted by the discontinuity in counterrotating orbits shown in Figs. 2.4, 2.5. The pathologies explained below are the reason why, in

Fig. 2.6, we only plotted the counterrotating edge of the region of validity when the Kerr spin parameter $|a| \leq 0.1$. Notice also that, when $N = 3$, the error regions in Fig. 2.6 are significantly larger than for any other N value.

Figure 2.7 clarifies the origin of the problem. When we use method ii), the top margin of the edge of the region of validity is estimated as the (smallest) value of $\bar{v}/v_{\rm ISCO}$ for which $\delta^{(3)}(\bar{v}) = \delta_0$. This condition corresponds to the leftmost intersection of the horizontal dashed red line with the solid black line in the plot. Similarly, we determine the most conservative estimate of the edge of the region of validity by considering the smallest v_l such that $\delta^{(3)}(v_l) = \delta_0/2$. This corresponds to the leftmost intersection of the horizontal, dot-dashed green line with the solid black line. For corotating orbits, as it happens, these intersections always exist. In fact, the local maximum in $\delta^{(3)}(v)$ (which is located at $v/v_{\rm ISCO} \sim 0.8$ for $a = 0$) moves to the *right* and becomes significantly larger as $a \to 1$. For counterrotating orbits the trend is the opposite: the local maximum moves to the left and decreases in magnitude. For a critical value of the spin $a \simeq -0.1$, the red dashed line and the solid black line do not intersect anymore. This is why in Figs. 2.4 and 2.5 we only plot the red-dashed (counterrotating) edge of the region of validity when $|a| \leq 0.1$. Of course, we can insist to identify $\bar{v}$ and v_l as the smallest values of v such that $\delta^{(3)}(\bar{v}) = \delta_0$, $\delta^{(3)}(v_l) = \delta_0/2$. This procedure leads to the red, dashed error bars in the $N = 3$ panel of Figs. 2.4 and 2.5. Note that these error bars are unnaturally small for $|a| > 0.4$.

Another possible solution would be to switch to method i) when method ii) fails. Now the upper margin of the edge of the region validity would be given by the first zero of $\delta^{(3)}(v)$, and the lower margin would be estimated by the condition given in Eq. (2.9). This results in the blue, dotted error bars shown in the central top panel of Figs. 2.4 and 2.5. These error bars are significantly more optimistic than the ones we presented in the rest of the paper, but (in our opinion) their significance is not as clear and well-justified as the rest of our results.

The problem discussed in this section concerns counterrotating orbits and $N = 3$.

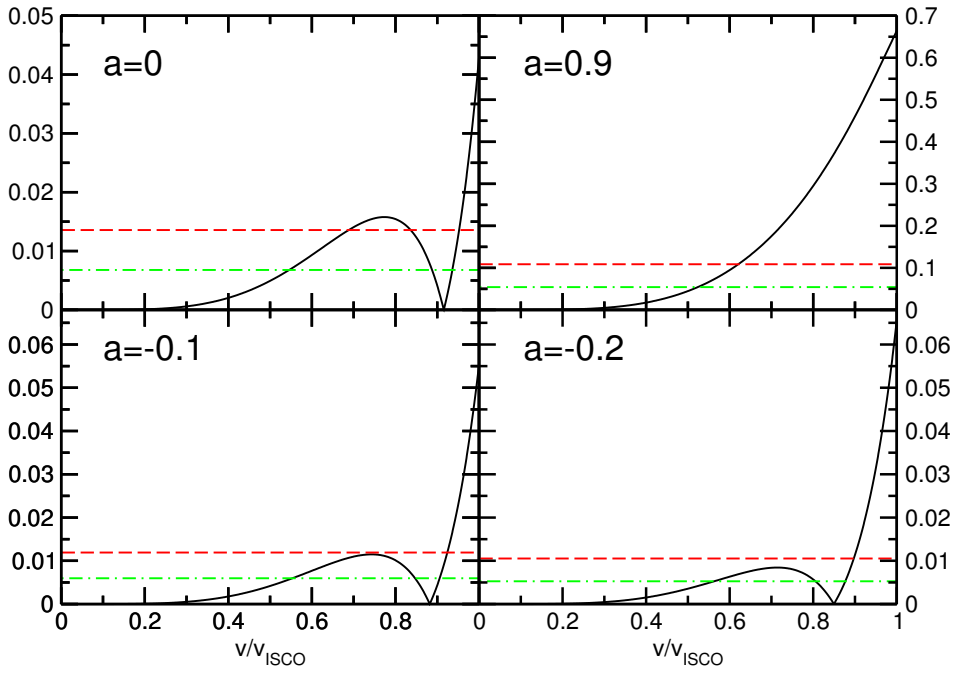

Figure 2.7

The solid black line shows $\delta^{(N)}(v)$ for $N = 3$. The horizontal dashed red (dot-dashed green) lines represent δ_0, computed from Eq. (2.10), and $\delta_0/2$. See text for discussion.

This is an exceptional case, and it does not affect the conclusions drawn earlier in the paper. However we should remark, for completeness, that similar pathologies occur for corotating orbits with $N = 6$ when $0 \leq a \leq 0.2$, and they may also occur at higher PN orders.

2.3 Relevance of multipolar components as a function of spin

Until now, we compared the PN approximation to numerical results that were considered to be virtually "exact". This was justified because the Teukolsky code computes as many multipoles in the angular decomposition of the radiation as needed to achieve an accuracy of $\mathcal{O}(10^{-10})$ at any given orbital velocity. While this is manageable in frequency-domain calculations, sometimes accurate calculations of a large number of multipoles are not possible in extreme mass-ratio *time-domain* codes, or in numerical relativity simulations of comparable-mass binaries: cf. Refs. [18, 17] for an analysis of multipolar decompositions of the radiation from comparable-mass binaries and Refs. [8, 7] for more recent numerical work

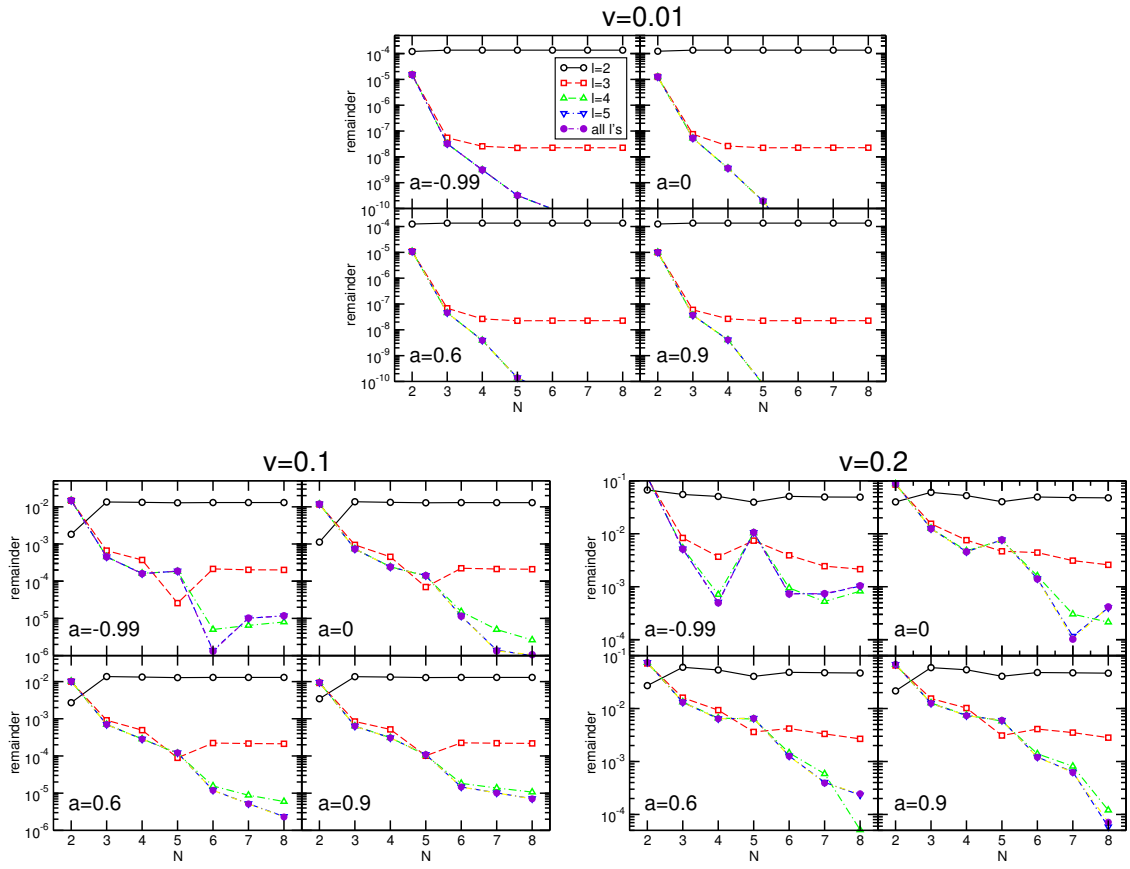

Figure 2.8

Relevance of multipolar components up to $\ell = 2$, $\ell = 3$, $\ell = 4$, $\ell = 5$, and summing as many ℓ's as necessary for the relative accuracy of the Teukolsky code to be $\mathcal{O}(10^{-10})$ at any given velocity.

to overcome these difficulties. As advocated in several papers [50, 61, 53, 47, 48, 49, 78], EMRIs provide a simple playground to study the number of multipolar components required to reach a given accuracy in the PN approximation (or in one of its resummed variants).

Figure 2.8 shows a comparison of the convergence of the multipolar decomposition versus the convergence of the PN expansion of the energy flux. This plot generalizes Fig. 7 of Ref. [50] in two ways: (i) it uses more accurate numerical data, and (ii) it considers the effect of the central BH spin on the number of multipolar components required to achieve a given accuracy.

We fix three values of the orbital velocity ($v = 0.01$, $v = 0.1$ and $v = 0.2$) and we

plot $F^{(\ell)} - F^{(N)}$, where $F^{(N)}$ is the Nth approximant of the PN energy flux and $F^{(\ell)}$ is the numerical energy flux truncated at the ℓth angular multipole. Some features are immediately visible from this plot:

(i) Even at low orbital velocities ($v = 0.01$), it is necessary to include multipolar components up to and including $\ell = 4$ to achieve an accuracy better than 10^{-7} in the flux; on the other hand, including up to $\ell = 5$ we obtain results that are as accurate as those that would be obtained including more multipoles.

(ii) For an orbital velocity $v = 0.1$ ($v = 0.2$) the best-known PN flux and numerical calculations always disagree at levels of $\sim 10^{-6}$ ($\sim 10^{-4}$) or larger. This is obviously due to the slower, nonmonotonic convergence of the PN approximation in this regime. Some nontrivial features of the PN approximation are again well-visible here: for example, as pointed out repeatedly in this paper, when $a = -0.99$ and $v = 0.1$ the 3PN ($N = 6$) expansion performs much better than higher-order expansions. This may well be accidental, and in fact it does not hold when $v = 0.2$, as then $N = 4$ is (most likely accidentally) better.

(iii) As a rule of thumb, the inclusion of multipoles up to and including $\ell = 5$ seems necessary to achieve the level of accuracy of the best-known ($N = 8$) PN expansion of the flux in the Kerr case. This conclusion is independent of the spin parameter a. In fact, a has hardly any effect on the number of multipolar components that must be included in the flux to achieve a desired accuracy.

CHAPTER 3

QUASINORMAL RINGING OF KERR BLACK HOLES

The gravitational radiation from a perturbed Kerr BH is usually described in terms of the Weyl scalar ψ_4 [51, 52], which can be decomposed in different multipolar components (say ψ_{lm}) by using spin-weighted spheroidal harmonics with angular indices $(l\,,m)$ (see, e.g., Ref. [16]). In the ringdown stage, each ψ_{lm} can be expressed as a sum of complex exponentials: schematically,

$$\psi_{lm} \sim \sum_{n=0}^{\infty} C_{lmn} \exp\left[-i\omega_{lmn}(t-r_*)\right] \,, \tag{3.1}$$

where the frequencies ω_{lmn} are complex, t denotes time as measured by an observer at infinity, r_* is a radial "tortoise" coordinate, and the index n ("overtone index") sorts the modes by increasing imaginary part ($n = 0$ corresponding to the smallest imaginary part and to the longest damping time). To simplify the notation, we will sometimes replace the indices $(l\,,m\,,n)$ by a collective index q.

The problem of extracting the QNM contribution to a generic signal was first studied in detail by Leaver [25]. The complex amplitudes C_q of each complex exponential, also called "excitation coefficients", depend on the source of the perturbation (see, e.g., Refs. [35, 15, 22]). The excitation coefficients can be factorized into the product $C_q = B_q I_q$ of a source-independent "excitation factor" B_q and of a source-dependent integral I_q. The integral I_q is in general divergent, but it can be regularized, yielding a finite answer in agreement with other perturbative calculations [25, 79, 55, 56].

To illustrate the origin of this factorization, consider the following prototypical ODE governing arbitrary perturbations around a BH. The perturbation is characterized by a wave

function Ψ with source Q (representing for example the perturbation due to infalling matter):

$$\frac{\partial^2}{\partial r_*^2}\Psi - \frac{\partial^2}{\partial t^2}\Psi - V\Psi = -Q(t)\,, \tag{3.2}$$

where r_* is a radial "tortoise coordinate", and the potential $V = V(r_*)$. The wave function Ψ can describe curvature-related quantities in the formalism by Sasaki and Nakamura [45] and it is directly related to metric perturbations in the Regge-Wheeler/Zerilli formalism [64, 26].

The QNM contribution to the time-domain Green's function G_Q reads

$$\Psi_Q(r_*, t) = \int_{-\infty}^{\infty}\int_{-\infty}^{\infty} G_Q(r_*, t|r'_*, t')Q(r'_*, t')dr'_*dt'\,,$$

where (see, e.g., Ref. [25])

$$\begin{aligned} & G_Q(r_*, t|r'_*, t') = \\ = \;& 2\mathrm{Re}\left[\sum_{q=0}^{\infty} B_q\psi_q(r_*)\psi_q(r'_*)e^{-i\omega_q(t-t'-r_*-r'_*)}\right]. \end{aligned} \tag{3.3}$$

The coefficients B_q are the (source-independent) *excitation factors*, and $\psi_q(r)$ denotes solutions of the homogeneous equation normalized such that $\psi_q(r) \to 1$ as $r_* \to \infty$. It is convenient to introduce also the source-dependent *excitation coefficients* C_q:

$$C_q = B_q I_q\,, \tag{3.4}$$

where

$$I_q \equiv \int_{-\infty}^{\infty} e^{i\omega_q r'_*}\psi_q(r'_*)q(r'_*, \omega)dr'_*\,, \tag{3.5}$$

and where the frequency-domain source term is

$$q(r'_*,\omega) = \int_{-\infty}^{\infty} e^{i\omega t'} Q(r'_*,t')dt' \,. \tag{3.6}$$

The calculation of the C_q's involves an integral in r_* from the horizon ($r_* = -\infty$) out to spatial infinity ($r_* = \infty$). The integral usually diverges at the horizon; one of the proposed methods to eliminate this divergence is discussed below in Section 3.2.3. With these definitions, the ringdown waveform can be written as:

$$\Psi(r_*,t) = 2\mathrm{Re}\left[\sum_{q=0}^{\infty} C_q \psi_q(r_*) e^{-i\omega_q(t-r_*)}\right] . \tag{3.7}$$

As $r_* \to \infty$ we have $\psi_q(r_*) \to 1$, so that

$$\Psi_Q(r_* \to \infty,t) = 2\mathrm{Re}\left[\sum_{q=0}^{\infty} C_q e^{-i\omega_q(t-r_*)}\right] . \tag{3.8}$$

To summarize, the complex excitation factors B_q are a "universal" intrinsic property of the BH which describes the excitability of each mode, independently of the source of the excitation. On the other hand, the complex excitation coefficients C_q are related to the amplitude of each QNM in response to a *specific* source inducing the oscillations.

In the first part of this chapter (Section 3.1) we compute a catalog of QNM excitation factors B_q for Kerr BHs using the formalism developed by Mano, Suzuki and Takasugi ([60, 59], henceforth MST). By using this technique we confirm and extend results obtained some years ago by Berti and Cardoso [9]. The main advantage of the MST method is that it does not require the (generally nontrivial) evaluation of Coulomb wave functions, which was instead necessary in Ref. [9]. This allows us to produce accurate tables of the B_q's for the modes that are most interesting in gravitational-wave detection (multipolar indices $l \leq 7$ and overtone indices $n = 0, \ldots, 4$). These tables (and similar tables for perturbations of spin

$s = 0$ and $s = 1$) were made publicly available on a website, along with a MATHEMATICA notebook that can be adapted to generate further tables if necessary [76].

In the rest of the chapter we compute the excitation coefficients C_q for a classic problem in perturbation theory: the calculation of the gravitational radiation emitted by particles falling into the BH. We generalize work carried out by Leaver more than 25 years ago [25] (see also Ref. [79]). Whereas Leaver considered only infalls from rest into a Schwarzschild BH, we present detailed comparisons between numerical waveforms and excitation coefficient calculations for particles falling with arbitrary energy into Schwarzschild BHs (Section 3.2) and we also consider the case where the BH is rotating (Section 3.3). In Section 4 we summarize our findings and point out possible directions for future work. Appendix 1 gives details about the regularization of divergent integrals in both the Schwarzschild and Kerr cases. We will use geometrical units ($G = c = 1$) throughout.

3.1 Excitation factors in the Mano-Suzuki-Takasugi formalism

In this Section we present a detailed calculation of the excitation factors B_q for Kerr QNMs. We follow the MST formalism [60] (see also Refs. [59, 58]) and we refer to the original papers for a more organic presentation of the material; our intention here is to give a practical guide to the calculation of the B_q's within this formalism. The method is different from – but equivalent to – Leaver's method [25], that was used by Berti and Cardoso in Ref. [9]. The main advantage of the MST formalism over Leaver's method is that the MST formalism does not require any (cumbersome) *evaluation* of Coulomb wave functions, as in Leaver's original treatment, but only a *matching* of the Coulomb-series expansion near infinity to an expansion in terms of hypergeometric functions near the horizon, which is simpler to perform in practice.

We will compute the excitation factors in both the Teukolsky and Sasaki-Nakamura formalisms (see Ref. [9] for a discussion). To begin with, let us define some quantities that

will be used below:

$$\begin{aligned} r_\pm &= M \pm \sqrt{M^2 - a^2}\,, \quad \kappa = \sqrt{1-j^2}\,, \\ x &= \frac{\omega(r_+ - r)}{\epsilon\kappa}\,, \quad \tau = \frac{\epsilon - am/M}{\kappa}\,, \quad \epsilon_\pm = \frac{\epsilon \pm \tau}{2}\,. \end{aligned} \tag{3.9}$$

From now on we follow Leaver's conventions and set $2M = 1$ (where M is the BH mass). In these units, the parameter $a \in [0,\, 1/2]$. In order to make contact with the more usual $M = 1$ units, we find it convenient to introduce a second dimensionless spin parameter $j \equiv 2a \in [0,\, 1]$. For reference, intermediate results of our calculations for a specific value of the spin ($a = 0.4$, or $j = 0.8$) are given in Table 3.1. In the remainder of this Section we will define and compute the quantities listed in this Table.

3.1.1 Computing ω_q and A_{lm}

In the Teukolsky formalism, the perturbations of a Kerr BH are described by the Newman-Penrose scalar ψ_4, which is related to solutions ϕ of the Teukolsky equation by $\phi \equiv \rho^{-4}\psi_4$, where $\rho = (r - ia\cos\theta)^{-1}$. By expanding in Fourier components

$$\rho^{-4}\psi_4 = \frac{1}{2\pi}\sum_{l=|s|}^{\infty}\sum_{m=-l}^{l}\int e^{-i\omega t + im\varphi} S_{lm\omega}(\theta) R_{lm\omega}(r)\, d\omega$$

and performing a separation of variables, one finds that the radial function $R_{lm\omega}$ and the angular function S_{lm} must satisfy the following equations:

$$\Delta\frac{d^2R_{lm\omega}}{dr^2} + (s+1)(2r-1)\frac{dR_{lm\omega}}{dr} + V(r)R_{lm\omega} = T_{lm\omega}\,, \tag{3.10}$$

$$\frac{d}{du}\left((1-u^2)\frac{dS_{lm}}{du}\right) + \left[a^2\omega^2u^2 - 2a\omega su + s + A_{lm} - \frac{(m+su)^2}{1-u^2}\right]S_{lm} = 0\,, \tag{3.11}$$

	$s=-2,\, l=m=2$	$s=-1,\, l=m=1$	$s=0,\, l=m=2$
ω_q	$1.172034 - 0.151259\,\mathrm{i}$	$0.701679 - 0.152621\,\mathrm{i}$	$1.41365 - 0.163041\,\mathrm{i}$
A_{lm}	$2.585294 + 0.205297\,\mathrm{i}$	$1.67659 + 0.0810074\,\mathrm{i}$	$5.95475 + 0.0106275\,\mathrm{i}$
ν	$-1.743843 - 0.701583\,\mathrm{i}$	$-1.69028 - 0.320182\,\mathrm{i}$	$-1.8012 - 0.0481726\,\mathrm{i}$
a_4^ν	-1.32616×10^{-3} $+1.43416\times10^{-3}\,\mathrm{i}$	-4.04792×10^{-3} $+3.01211\times10^{-3}\,\mathrm{i}$	-0.229461 $-0.0295086\,\mathrm{i}$
a_{-4}^ν	-4.52814×10^{-3} $-2.12986\times10^{-2}\,\mathrm{i}$	8.02490×10^{-5} $-2.25538\times10^{-4}\,\mathrm{i}$	1.47272×10^{-3} $+3.40832\times10^{-4}\,\mathrm{i}$
K_ν	1.06144×10^{-3} $+7.43631\times10^{-4}\,\mathrm{i}$	-0.0812872 $+0.0682523\,\mathrm{i}$	-12.0419 $+1.20138\,\mathrm{i}$
$K_{-\nu-1}$	-8.19837×10^{-2} $-9.20267\times10^{-1}\,\mathrm{i}$	$1.55992 + 1.23780\,\mathrm{i}$	$18.6581 + 3.85088\,\mathrm{i}$
$B^{\mathrm{inc}}_{lm\omega}$	-2.80111×10^{-16} $+3.11473\times10^{-16}\,\mathrm{i}$	-4.51443×10^{-15} $-2.05141\times10^{-15}\,\mathrm{i}$	6.08313×10^{-14} $+1.91604\times10^{-14}\,\mathrm{i}$
$B^{\mathrm{ref}}_{lm\omega}$	$3.16122 + 1.25413\,\mathrm{i}$	$1.59262 - 0.363221\,\mathrm{i}$	$1.27738 + 0.760771\,\mathrm{i}$
$B^{\mathrm{trans}}_{lm\omega}$	$15.4151 + 11.0126\,\mathrm{i}$	$3.32227 + 0.409647\,\mathrm{i}$	$0.496587 + 1.24305\,\mathrm{i}$
α_q^{T}	$0.114759 - 0.241821\,\mathrm{i}$	$-1.25046 - 1.01565\,\mathrm{i}$	$-0.154117 - 3.58899\,\mathrm{i}$
B_q^{T}	$-0.240807 + 0.150102\,\mathrm{i}$	$-0.153477 - 0.144681\,\mathrm{i}$	$-0.0955564 + 0.0516867\,\mathrm{i}$
B_q^{SN}	-0.0911231 $+0.0613455\,\mathrm{i}$	-0.0298959 $-0.119248\,\mathrm{i}$	-0.0955564 $+0.0516867\,\mathrm{i}$

Table 3.1

Some intermediate quantities necessary to compute the excitation factors for the fundamental mode ($n=0$) of a Kerr BH with $a=0.4$ (or $j=0.8$). The three columns refer to gravitational ($s=-2$) perturbations with $l=m=2$, electromagnetic ($s=-1$) perturbations with $l=m=1$, and scalar ($s=0$) perturbations with $l=m=2$.

where $u=\cos\theta$ and $T_{lm\omega}$ is the Fourier transform of the stress-energy tensor after separation of the angular dependence. The potential $V(r)$ is given by

$$\begin{aligned} V(r) &= \left\{(r^2+a^2)^2\omega^2 - 2am\omega r + a^2m^2 \right. \\ &+ \left. is\left[am(2r-1) - \omega(r^2-a^2)\right]\right\}\Delta^{-1} \\ &+ 2is\omega r - a^2\omega^2 - A_{lm}\,, \end{aligned} \tag{3.12}$$

where A_{lm} is the angular separation constant corresponding to the angular eigenfunctions S_{lm} (known as "spin-weighted spheroidal harmonics"). The eigenfrequency $\omega_{lmn}=\omega_q$ and the angular eigenvalue A_{lm} are determined by imposing QNM boundary conditions on the

radial equation (3.10) and regularity conditions on the angular equation (3.11): see, e.g., Ref. [12]. The radial and angular equations are solved via a series solution whose coefficients b_n^r and b_n^θ satisfy three-term recursion relations of the form

$$\begin{aligned} \alpha_0^\theta b_1^{(r,\theta)} + \beta_0^{(r,\theta)} b_0^{(r,\theta)} &= 0\,, \\ \alpha_n^{(r,\theta)} b_{n+1}^{(r,\theta)} + \beta_n^{(r,\theta)} b_n^{(r,\theta)} + \gamma_n^{(r,\theta)} b_{n-1}^{(r,\theta)} &= 0\,, \end{aligned} \tag{3.13}$$

where the superscript (r or θ) denotes association with the radial or angular equation, and the coefficients of the three-term recursion relations can be found in Ref. [24].

By the principle of minimal solutions, the convergence of the series obtained via the three-term recursion relations is guaranteed by two continued fraction relations (one coming from the radial series expansion, the other from the angular series expansion) of the form

$$\beta_0^\theta = \frac{\alpha_0^\theta \gamma_1^\theta}{\beta_1^\theta - \frac{\alpha_1^\theta \gamma_2^\theta}{\beta_2^\theta - \ldots}}\,, \tag{3.14}$$

$$\beta_0^r = \frac{\alpha_0^r \gamma_1^r}{\beta_1^r - \frac{\alpha_1^r \gamma_2^r}{\beta_2^r - \ldots}}\,. \tag{3.15}$$

or by any of their inversions, which are analytically – but not numerically – equivalent [24].

We now have two complex equations, (3.14) and (3.15), in two complex unknowns, ω_q and A_{lm}. By solving these equations numerically we find the eigenvalues listed in the first two rows of Table 3.1. Numerical practice shows that the qth inversion index for the radial equation is best suited for numerical searches of the qth overtone ω_q. Numerical experimentation (and analytical arguments [16]) show that the optimal inversion number to find the angular eigenvalue with the correct limit as $a \to 0$, i.e.,

$$A_{lm} \to l(l+1) - s(s+1)\,, \tag{3.16}$$

is equal to $l - \max(|m|, |s|)$.

3.1.2 Angular momentum parameter ν and matching function K_ν

The basic idea of the MST method is to (1) find a first independent solution of the radial equation R_0^ν in terms of a series of hypergeometric functions (which does not converge at spatial infinity) with expansion coefficients proportional to a_n^ν, cf. Eq. (2.21) of Ref. [60]; (2) consider Leaver's construction of a series of Coulomb wave functions R_C^ν that is valid near infinity; (3) notice that the two solutions are identical modulo a ν-dependent constant, i.e.,

$$R_0^\nu = K_\nu R_C^\nu \,. \tag{3.17}$$

The expansion coefficients a_n^ν and the matching condition depend on an "angular momentum" parameter ν which appears in the three-term recurrence relation

$$\alpha_n^\nu a_{n+1}^\nu + \beta_n^\nu a_n^\nu + \gamma_n^\nu a_{n-1}^\nu = 0 \,, \tag{3.18}$$

where

$$\begin{aligned}
\alpha_n^\nu &= \frac{i\epsilon\kappa(n+\nu+1+s+i\epsilon)(n+\nu+1+s-i\epsilon)}{(n+\nu+1)(2n+2\nu+3)(n+\nu+1+i\tau)^{-1}} \,, \\
\beta_n^\nu &= -\lambda - s(s+1) + (n+\nu)(n+\nu+1) + \epsilon^2 \\
&+ \epsilon(\epsilon - mq) + \frac{\epsilon(\epsilon-mq)(s^2+\epsilon^2)}{(n+\nu)(n+\nu+1)} \,, \\
\gamma_n^\nu &= -\frac{i\epsilon\kappa(n+\nu-s+i\epsilon)(n+\nu-s-i\epsilon)}{(n+\nu)(2n+2\nu-1)(n+\nu-i\tau)^{-1}} \,.
\end{aligned} \tag{3.19}$$

and λ is related to the separation constant A_{lm} by

$$\lambda = A_{lm} + (a\omega)^2 - 2am\omega \,. \tag{3.20}$$

The solution of the above recursion relation is "minimal" (i.e., the a_n^ν's give rise to a convergent series) if

$$\beta_0^\nu = \frac{\alpha_{-1}^\nu \gamma_0^\nu}{\beta_{-1}^\nu - \frac{\alpha_{-2}^\nu \gamma_{-1}^\nu}{\beta_{-2}^\nu - \ldots}} + \frac{\alpha_0^\nu \gamma_1^\nu}{\beta_1^\nu - \frac{\alpha_1^\nu \gamma_2^\nu}{\beta_2^\nu - \ldots}} \,. \tag{3.21}$$

This condition is only satisfied by a discrete set of (complex) values of ν. Different inversions of Eq. (3.21) yield different values of ν: for example, we could consider the first inversion

$$\beta_1^\nu = \frac{\alpha_0^\nu \gamma_1^\nu}{\beta_0^\nu - \frac{\alpha_{-1}^\nu \gamma_0^\nu}{\beta_{-1}^\nu - \frac{\alpha_{-2}^\nu \gamma_{-1}^\nu}{\beta_{-2}^\nu - \ldots}}} + \frac{\alpha_1^\nu \gamma_2^\nu}{\beta_2^\nu - \ldots} \tag{3.22}$$

or even a sequence of "negative" inversions, such as

$$\beta_{-1}^\nu = \frac{\alpha_{-2}^\nu \gamma_{-1}^\nu}{\beta_{-2}^\nu - \ldots} + \frac{\alpha_{-1}^\nu \gamma_0^\nu}{\beta_0^\nu - \frac{\alpha_0^\nu \gamma_1^\nu}{\beta_1^\nu - \frac{\alpha_1^\nu \gamma_2^\nu}{\beta_2^\nu - \ldots}}} \,. \tag{3.23}$$

Inversions are useful also for the radial and angular continued fractions, but the numerical calculation of ν is a little trickier: the numerical root ν can be different for different inversions of the continued fraction, but this does not affect the physics of the problem. The reason is that the eigenvalues ν have the following properties: (i) ν has period equal to 1: if ν is a solution, $\nu \pm 1$ is also a solution; (ii) If ν is a solution, $-\nu$ is also a solution.

Given the eigenvalue ν (as listed, e.g., in the third row of Table 3.1), it is straightforward to build up the series coefficients a_n^ν from the three-term recursion relation (3.18). If we choose the arbitrary normalization constant such that $a_0^\nu = 1$, we get (for example) the values of a_4^ν and a_{-4}^ν listed in rows four and five of Table 3.1.

An important property of these coefficients is that $a_{-n}^{-\nu-1} = a_n^\nu$: this can be shown starting from the three-term recursion relation (3.18), and using Eqs. (3.19). Therefore we can denote them by a_n^ν when they refer to K_ν, and by $a_{-n}^{-\nu-1}$ when they refer to $K_{-\nu-1}$.

As we will see below, to obtain the QNM excitation coefficients we must compute K_ν and $K_{-\nu-1}$, given by Eq. (165) in Ref. [44]:

$$\begin{aligned} K_\nu &= \frac{e^{i\epsilon\kappa}(2\epsilon\kappa)^{s-\nu-p}2^{-s}i^p\Gamma(1-s-2i\epsilon_+)\Gamma(p+2\nu+2)}{\Gamma(p+\nu+1-s+i\epsilon)\Gamma(p+\nu+1+i\tau)\Gamma(p+\nu+1+s+i\epsilon)} \\ &\times \left(\sum_{n=-\infty}^{p}\frac{(-1)^n}{(p-n)!(p+2\nu+2)_n\frac{(\nu+1+s-i\epsilon)_n}{(\nu+1-s+i\epsilon)_n}}a_n^\nu\right)^{-1} \\ &\times \left(\sum_{n=p}^{\infty}\frac{\Gamma(n+p+2\nu+1)}{(-1)^n(n-p)!}\frac{\Gamma(n+\nu+1+s+i\epsilon)}{\Gamma(n+\nu+1-s-i\epsilon)}\frac{\Gamma(n+\nu+1+i\tau)}{\Gamma(n+\nu+1-i\tau)}a_n^\nu\right), \end{aligned} \tag{3.24}$$

where the notation $(x)_n$ is a shorthand for the following function of x:

$$(x)_n \equiv \frac{\Gamma(x+n)}{\Gamma(x)}, \tag{3.25}$$

and p can be any integer. Both K_ν and $K_{-\nu-1}$ are independent of the choice of p; indeed, this property can be used as a check of the calculation. Representative values of K_ν and $K_{-\nu-1}$ are listed in Table 3.1.

3.1.3 Amplitudes $B^{\rm inc}_{lm\omega}$, $B^{\rm ref}_{lm\omega}$ and $B^{\rm trans}_{lm\omega}$ in the Teukolsky formalism

According to Eqs. (167), (168) and (169) in Ref. [44], the ingoing-wave radial solution has the asymptotic behavior

$$R^{\rm in}_{lm\omega} \to \begin{cases} B^{\rm trans}_{lm\omega}\Delta^2 e^{-ikr^*} \text{ as } r\to r_+, \\ r^3 B^{\rm ref}_{lm\omega}e^{i\omega r^*} + r^{-1}B^{\rm inc}_{lm\omega}e^{-i\omega r^*} \text{ as } r\to+\infty, \end{cases} \tag{3.26}$$

where the amplitudes are defined as:

$$\begin{aligned} B^{\rm inc}_{lm\omega} &= \omega^{-1}\left(K_\nu - ie^{-i\pi\nu}\frac{\sin\pi(\nu-s+i\epsilon)}{\sin\pi(\nu+s-i\epsilon)}K_{-\nu-1}\right)A^\nu_+ \\ &\times \quad e^{-i\ \epsilon\ln\epsilon}\,, \end{aligned} \tag{3.27}$$

$$B^{\rm ref}_{lm\omega} = \omega^{-1-2s}\left(K_\nu + ie^{i\pi\nu}K_{-\nu-1}\right)A^\nu_- e^{i\ \epsilon\ln\epsilon}\,, \tag{3.28}$$

$$B^{\rm trans}_{lm\omega} = \left(\frac{\epsilon\kappa}{\omega}\right)^{2s} e^{i\epsilon_+\ln\kappa}\sum_{n=-\infty}^{\infty} a^\nu_n\,, \tag{3.29}$$

and

$$\begin{aligned} A^\nu_+ &= e^{-(\pi/2)\epsilon}e^{(\pi/2)i(\nu+1-s)}2^{-1+s-i\epsilon} \\ &\times \quad \frac{\Gamma(\nu+1-s+i\epsilon)}{\Gamma(\nu+1+s-i\epsilon)}\sum_{n=-\infty}^{\infty} a^\nu_n\,, \end{aligned} \tag{3.30}$$

$$\begin{aligned} A^\nu_- &= e^{-(\pi/2)\epsilon}e^{-(\pi/2)i(\nu+1+s)}2^{-1-s+i\epsilon} \\ &\times \quad \sum_{n=-\infty}^{\infty}(-1)^n\frac{(\nu+1+s-i\epsilon)_n}{(\nu+1-s+i\epsilon)_n}a^\nu_n\,. \end{aligned} \tag{3.31}$$

The QNM boundary conditions require that $B^{\rm inc}_{lm\omega}$ must vanish at the QNM frequencies ω_q. Table 3.1 shows that this indeed happens within an accuracy very close to machine precision. The table also lists reference values for $B^{\rm ref}_{lm\omega}$ and $B^{\rm trans}_{lm\omega}$.

3.1.4 $\alpha^{\rm T}_q$ in the Teukolsky formalism

The excitation factors (in the Teukolsky formalism) are defined as

$$B^{\rm T}_q = -\frac{A^{\rm T}_{\rm out}(\omega_q)}{2i\omega_q\alpha^{\rm T}_q}\,. \tag{3.32}$$

Here

$$\alpha^{\rm T}_q \equiv i\left(\frac{dA^{\rm T}_{in}}{d\omega}\right)_{\omega_q}\,, \tag{3.33}$$

and furthermore

$$A^{\rm T}_{\rm in} \equiv \frac{B^{\rm inc}_{lm\omega}}{B^{\rm trans}_{lm\omega}}\,, \quad A^{\rm T}_{\rm out} \equiv \frac{B^{\rm ref}_{lm\omega}}{B^{\rm trans}_{lm\omega}}\,. \tag{3.34}$$

Note that we can divide both $B^{\rm inc}_{lm\omega}$ and $B^{\rm ref}_{lm\omega}$ by some arbitrary function $G(\omega)$ without affecting the excitation factors $B^{\rm T}_q$. This is because $B^{\rm inc}_{lm\omega}$ must vanish at the QNM frequencies ω_q, so $G(\omega)$ is just an arbitrary rescaling (or normalization) factor. The proof is trivial:

$$B^{\rm T}_q \propto \left(\frac{B^{\rm ref}_{lm\omega}}{dB^{\rm inc}_{lm\omega}/d\omega}\right)_{\omega_q} = \left(\frac{B^{\rm ref}_{lm\omega}/G}{d[B^{\rm inc}_{lm\omega}/G]/d\omega}\right)_{\omega_q}\,. \tag{3.35}$$

The simplest choice would be to set $G = 1$, but in order to reproduce all of the values listed in Leaver's Table I [25], especially $\alpha^{\rm SN}_q$ and $A^{\rm SN}_{\rm out}$, we choose a normalization factor

$$G = B^{\rm trans}_{lm\omega}\,. \tag{3.36}$$

To get $\alpha^{\rm T}_q$ we must compute the derivative of $A^{\rm T}_{\rm in}$ with respect to ω. We first compute $A^{\rm T}_{\rm in}$ at the QNM frequency ω_q, $A^{\rm T}_{\rm in}(\omega_q)$. Then we consider a new frequency $\omega_q + \delta$, and we repeat the calculation described above to get $A^{\rm T}_{\rm in}(\omega_q + \delta)$; note in particular that when we repeat the first step (as described in Section 3.1.1) we use the angular continued fraction to obtain a "new" angular constant, evaluated at $\omega_q + \delta$. Finally we can compute the derivative by finite differencing:

$$\alpha^{\rm T}_q = i\frac{A^{\rm T}_{\rm in}(\omega_q + \delta) - A^{\rm T}_{\rm in}(\omega_q)}{\delta}\,. \tag{3.37}$$

In our calculation we set $\delta = 10^{-7}$ (i.e., we differentiate along the real axis); as a check of our finite-differencing procedure we also repeat the calculation with $\delta = 10^{-7}i$ (i.e., differentiating along the pure-imaginary axis). The two results usually agree to better than one part in 10^6.

3.1.5 Excitation factors in the Teukolsky ($B_q^{\rm T}$) and Sasaki-Nakamura ($B_q^{\rm SN}$) formalisms

The excitation factors in the Teukolsky formalism were defined in Eq. (3.32). It turns out that for many practical purposes, including the calculation of radiation from infalling point particles that will be presented later on in this paper, it is more convenient to use the Sasaki-Nakamura wave function X, related to Teukolsky's by

$$X = \frac{\sqrt{r^2+a^2}}{\Delta}\left(\alpha(r)R + \frac{\beta(r)}{\Delta}R'\right), \tag{3.38}$$

where the prime stands for a derivative with respect to r. Specializing to the case presented in Appendix B of Sasaki and Nakamura [45] [i.e, $f = h = 1$ and $g = (r^2+a^2)/r^2$], the functions α and β are, respectively:

$$\alpha = -\frac{iK}{\Delta^2}\beta + 3iK' + \lambda + \frac{6\Delta}{r^2}, \tag{3.39}$$

$$\beta = \Delta\left[-2iK + \Delta' - 4\frac{\Delta}{r}\right]. \tag{3.40}$$

Here $K = (r^2+a^2)\omega - am$, $\Delta = r^2 - 2Mr + a^2$ and λ was defined in Eq. (3.20). Then the Sasaki-Nakamura wave function X satisfies

$$\frac{d^2X}{dr_*^2} - \mathcal{F}\frac{dX}{dr_*} - \mathcal{U}X = \mathcal{S}, \tag{3.41}$$

where the tortoise coordinate is defined as $\frac{dr}{dr_*} = \frac{r^2+a^2}{\Delta}$. The tortoise coordinate is defined up to an integration constant, which we fix once and for all by setting

$$r_* = r + \frac{2Mr_+}{r_+ - r_-}\log(r - r_+) - \frac{2Mr_-}{r_+ - r_-}\log(r - r_-). \tag{3.42}$$

The functions $\mathcal{F}$ and $\mathcal{U}$ are given by

$$\begin{aligned}
\mathcal{F} &= \frac{\Delta}{r^2+a^2}F\,, \quad F \equiv \frac{\gamma'}{\gamma}\,,\\
\gamma &\equiv \alpha\left(\alpha+\frac{\beta'}{\Delta}\right)-\frac{\beta}{\Delta}\left(\alpha'-\frac{\beta}{\Delta^2}V\right)\,,\\
\mathcal{U} &= \frac{\Delta U}{(r^2+a^2)^2}+G^2+\frac{dG}{dr_*}-\frac{\Delta GF}{r^2+a^2}\,,\\
G &\equiv -\frac{\Delta'}{r^2+a^2}+\frac{r\Delta}{(r^2+a^2)^2}\,,\\
U &= -V+\frac{\Delta^2}{\beta}\left[\left((2\alpha+\frac{\beta'}{\Delta}\right)'-\frac{\gamma'}{\gamma}\left(\alpha+\frac{\beta'}{\Delta}\right)\right]\,.
\end{aligned}$$

Note that our Teukolsky potential V differs by an overall minus sign from the potential used by Sasaki and Nakamura, and that

$$\lim_{r\to\infty}\gamma \equiv \gamma_\infty = \lambda(2+\lambda)-12iM\omega-12a\omega\left(\omega a-m\right)\,. \tag{3.43}$$

When $a\to 0$ the Sasaki-Nakamura potential reduces, by construction, to the so-called Regge-Wheeler potential (cf. Section 3.2 below for more details). The asymptotic behavior of the Sasaki-Nakamura wave function is

$$X \sim A_{\rm trans}e^{-ikr_*}\,, \quad r\to r_+\,, \tag{3.44}$$

$$X \sim A_{\rm in}e^{-i\omega r_*}+A_{\rm out}e^{i\omega r_*}\,, \quad r\to\infty\,. \tag{3.45}$$

where $k=\omega-am/r_+$, and the coefficients can be related to the corresponding Teukolsky coefficients by

$$A^{\rm T}_{\rm in} = -\frac{1}{4\omega^2}A_{\rm in}\,, \tag{3.46}$$

$$A^{\rm T}_{\rm out} = -\frac{4\omega^2}{\lambda(\lambda+2)-6i\omega-12a\omega(a\omega-m)}A_{\rm out}\,, \tag{3.47}$$

and $\lambda \equiv A_{lm} + (a\omega)^2 - 2am\omega$. The normalization at the horizon is such that

$$\begin{aligned} A_{\rm trans} &= r_+^{1/2}\left[(8 - 12i\omega - 4\omega^2)r_+^2\right. \\ &+ (12iam - 8 + 8am\omega + 6i\omega)r_+ \\ &- \left. 4a^2m^2 - 6iam + 2\right]. \end{aligned} \tag{3.48}$$

A change of wave function of the form

$$X = \exp\left[\int \frac{\mathcal{F}}{2} dr_*\right] X_2 = X_2\sqrt{\gamma} \tag{3.49}$$

eliminates the first derivative, yielding

$$\frac{d^2X_2}{dr_*^2} + \left(\frac{\mathcal{F}'}{2} - \frac{\mathcal{F}^2}{4} - \mathcal{U}\right) X_2 = \mathcal{S}\exp\left[-\int \frac{\mathcal{F}}{2} dr_*\right] = \frac{\mathcal{S}}{\sqrt{\gamma}}\,. \tag{3.50}$$

To get the excitation factors in the Sasaki-Nakamura formalism we only need the asymptotic relation between X and R, Eq. (3.47) (similar relations are presented in Ref. [9] for scalar and electromagnetic perturbations). Denoting scalar, electromagnetic and gravitational perturbations by the subscript 0, -1 and -2 respectively, and dropping the "q" subscripts to simplify the notation, we have:

$$B_0^{\rm SN} = B_0^{\rm T}\,, \tag{3.51}$$

$$B_{-1}^{\rm SN} = -\frac{2am\omega_q - A_{lm} - a^2\omega_q^2}{4\omega_q^2} B_{-1}^{\rm T}\,, \tag{3.52}$$

$$B_{-2}^{\rm SN} = \frac{\lambda(\lambda+2) - 6i\omega_q - 12a\omega_q(a\omega_q - m)}{16\omega_q^4} B_{-2}^{\rm T}\,. \tag{3.53}$$

The results for $a = 0.4$ ($j = 0.8$) are listed in the last row of Table 3.1. All of the B_q's (for $s = 0\,, -1\,, -2$) match the results of Paper I, but now the computation does not involve tricky evaluations of the Coulomb wave functions. This allows us to compute excitation factors for a larger range of spin values, and for a larger set of values of $(l\,, m)$

and of the overtone number n. An extensive catalog of results for Kerr perturbations of spin $s = 0$, 1 and 2, $l = s, \ldots, 7$ and $n = 0, \ldots, 3$ is provided online in the form of downloadable numerical tables [76].

3.2 Excitation factors and excitation coefficients for Schwarzschild black holes

3.2.1 Excitation factors for the Zerilli and Regge-Wheeler equations

Perturbations of rotating (Kerr) BHs are conveniently described using curvature-related quantities in the Newman-Penrose approach. As discussed in the previous section, this naturally leads to the definition of the excitation factors in either the Teukolsky or Sasaki-Nakamura formalism (the latter being more suitable to numerical calculations, due to the short-range nature of the source term of the Sasaki-Nakamura equation).

For the Schwarzschild BH geometry, a (perhaps more physically transparent) direct metric perturbation treatment can be performed. The perturbations separate in two sectors depending on their behavior under parity: the axial (or odd) and polar (or even) sector. Odd-parity metric perturbations can be found from the Regge-Wheeler wave function $\Psi^{(-)}$, and even-parity perturbations lead to the Zerilli equation for a single wave function $\Psi^{(+)}$. In both cases the problem reduces to the solution of a wave equation of the form

$$\frac{\partial^2}{\partial r_*^2}\Psi^{(\pm)} - \frac{\partial^2}{\partial t^2}\Psi^{(\pm)} - V^{(\pm)}\Psi^{(\pm)} = -Q^{(\pm)}(t)\,. \tag{3.54}$$

Defining $\lambda = (l-1)(l+2)/2$, the Zerilli potential reads

$$V^{(+)} = \left(\frac{r-1}{r}\right)\frac{8\lambda^2(\lambda+1)r^3 + 12\lambda^2 r^2 + 18\lambda r + 9}{r^3(2\lambda r+3)^2}\,, \tag{3.55}$$

whereas the Regge-Wheeler potential reads

$$V^{(-)} = \frac{r-1}{r^3}\left[l(l+1) - \frac{3}{r}\right]\,. \tag{3.56}$$

These equations can be solved in the frequency domain using the approach followed by Leaver [25] and summarized below. At the QNM frequencies, the Regge-Wheeler wave function, normalized such that $\psi_q^{(-)}(r) \to 1$ as $r \to \infty$, reads:

$$\begin{aligned}\psi_q^{(-)}(r) &= \left(1-\frac{1}{r}\right)^{-2i\omega_q}\left[\sum_{n=0}^{\infty} a_n(\omega_q)\right]^{-1} \\ &\times \left[\sum_{n=0}^{\infty} a_n(\omega_q)(1-1/r)^n\right], \end{aligned} \tag{3.57}$$

where the coefficients a_n can be computed from a three-term recursion relation (cf. Appendix A in Ref. [25]). A simple relation between the homogeneous solutions of the Zerilli and Regge-Wheeler equation was found by Chandrasekhar [54] (see also Eqs. (102)-(104) in Ref. [25]). Using the Chandrasekhar transformation, we find that the Zerilli wave function $\psi_q^{(+)}(r)$, again normalized such that $\psi_q^{(+)}(r) \to 1$ as $r \to \infty$, is

$$\begin{aligned}\psi_q^{(+)}(r) &= \frac{(1-1/r)^{-2i\omega_q}}{\sum a_n}\sum_{n=0}^{\infty}\left(1+\frac{-6i\omega_q(2\lambda r+3)+9(r-1)}{r^2(2\lambda r+3)[2\lambda(\lambda+1)+3i\omega_q]} + \right. \\ &\left. + \frac{3n}{r^2\left[2\lambda(\lambda+1)+3i\omega_q\right]}\right)\times a_n\left(\frac{r-1}{r}\right)^n. \end{aligned} \tag{3.58}$$

As explained at the beginning of this chapter, the QNM contribution to the time-domain Green's function reads

$$\Psi_Q^{(\pm)}(r_*,t) = \int_{-\infty}^{\infty}\int_{-\infty}^{\infty} G_Q^{(\pm)}(r_*,t|r'_*,t')Q^{(\pm)}(r'_*,t')dr'_*dt' \,,$$

with

$$\begin{aligned} & G_Q(r_*,t|r'_*,t') = \\ &= 2\mathrm{Re}\left[\sum_{q=0}^{\infty} B_q^{(\pm)}\psi_q^{(\pm)}(r)\psi_q^{(\pm)}(r')e^{-i\omega_q(t-t'-r_*-r'_*)}\right]. \end{aligned} \tag{3.59}$$

Because the Sasaki-Nakamura wave function reduces to the Regge-Wheeler wave func-

$B_q^{(-)}$	$l=2$	$l=3$	$l=4$	$l=5$
$n=0$	0.126902 $+0.0203152\,\mathrm{i}$	-0.0938898 $-0.0491928\,\mathrm{i}$	0.065348 $+0.0652391\,\mathrm{i}$	-0.0384465 $-0.0735239\,\mathrm{i}$
$n=1$	0.0476826 $-0.223755\,\mathrm{i}$	-0.151135 $+0.269750\,\mathrm{i}$	0.261488 $-0.251524\,\mathrm{i}$	-0.363440 $+0.182660\,\mathrm{i}$
$n=2$	-0.190284 $+0.0157486\,\mathrm{i}$	0.415029 $+0.141038\,\mathrm{i}$	-0.549217 $-0.435328\,\mathrm{i}$	0.534171 $+0.828615\,\mathrm{i}$
$n=3$	0.0808676 $+0.0796126\,\mathrm{i}$	-0.0434028 $-0.412747\,\mathrm{i}$	-0.316921 $+0.837911\,\mathrm{i}$	1.08630 $-1.14858\,\mathrm{i}$
$B_q^{(+)}$	$l=2$	$l=3$	$l=4$	$l=5$
$n=0$	0.120923 $+0.0706696\,\mathrm{i}$	-0.0889796 $-0.0611757\,\mathrm{i}$	0.0621266 $+0.069100\,\mathrm{i}$	-0.0364029 $-0.0748073\mathrm{i}$
$n=1$	0.158645 $-0.253334\,\mathrm{i}$	-0.191928 $+0.264820\,\mathrm{i}$	0.279700 $-0.241825\mathrm{i}$	-0.371542 $+0.173592\,\mathrm{i}$
$n=2$	-0.298933 $-0.0711341\,\mathrm{i}$	0.436786 $+0.204560\,\mathrm{i}$	-0.543211 $-0.478060\,\mathrm{i}$	0.517754 $+0.854935\,\mathrm{i}$
$n=3$	0.113837 $+0.204137\,\mathrm{i}$	-0.000920468 $-0.476365\,\mathrm{i}$	-0.374502 $+0.859526\,\mathrm{i}$	1.13916 $-1.14048\,\mathrm{i}$

Table 3.2

Odd- and even-parity excitation factors for $l = 2\,, 3\,, 4\,, 5$.

tion when $a \to 0$, the corresponding excitation factors are related by

$$B_q^{(-)} = B_{-2}^{\mathrm{SN}}(a=0)\,. \tag{3.60}$$

The even-parity excitation factors $B_q^{(+)}$ are related to the odd-parity excitation factors $B_q^{(-)}$ by [54, 25]

$$B_q^{(+)} = B_q^{(-)} \frac{2\lambda(\lambda+1) + 3i\omega_q}{2\lambda(\lambda+1) - 3i\omega_q}\,. \tag{3.61}$$

Thus, one can compute excitation factors for both the Regge-Wheeler and Zerilli representations using the excitation factors computed in Section 3.1.

For completeness, in Table 3.2 we list the axial ($B_q^{(-)}$) and polar ($B_q^{(+)}$) Schwarzschild excitation factors for the fundamental mode and for the first three overtones with $l = 2$, 3, 4,

5. From Table 3.2 we see that the absolute values of the excitation factors $|B_q^{(+)}|$ for different overtone numbers n and fixed l are of comparable magnitude. Values of these coefficients up to $l = 7$ can be computed using the data available in Ref. [76].

3.2.2 Excitation coefficients for low- and high-energy particle infalls

We will now compute the source-dependent excitation *coefficients* C_q and compare them with actual waveforms for head-on infalls into Schwarzschild or Kerr BHs along the symmetry axis. This is a classic problem addressed via the Regge-Wheeler-Zerilli formalism for non-rotating BHs [43] and via the Sasaki-Nakamura formalism for Kerr BHs [45]. The original analysis was revisited by several authors, who considered particles falling with generic energy and from finite distance into Schwarzschild BHs, Kerr BHs, and higher-dimensional BHs [74, 4, 70, 72, 31, 10, 19, 13, 21]. In four dimensions, head-on collisions with large mass ratio have even become accessible to simulations in full numerical relativity [68, 75].

In general, the source-dependent excitation coefficients $C_q^{(\pm)}$ are given by

$$C_q^{(\pm)} = B_q^{(\pm)} I_q^{(\pm)} \,, \tag{3.62}$$

where

$$I_q^{(\pm)} \equiv \int_1^\infty e^{i\omega_q r'} \psi_q^{(\pm)}(r') q^{(\pm)}(r', \omega)(r'-1)^{i\omega_q - 1} r' dr' \,, \tag{3.63}$$

and where $q^{(\pm)}(r', \omega)$ denotes the frequency-domain source term. The calculation of the $C_q^{(\pm)}$'s involves an integral in r from the horizon ($r = 1$) out to spatial infinity ($r = \infty$). The integral usually diverges at the horizon, but this divergence can be eliminated, as discussed below.

For a four-dimensional Schwarzschild BH, radial infalls excite only even (polar) per-

turbations and the source term in the Fourier domain reads

$$\begin{aligned} q(r,\omega) &= m_0 4\sqrt{2\pi}\sqrt{4l+2}\,\frac{r-1}{r(2\lambda r+3)} \\ &\times \left[\left(E^2-1+\frac{1}{r}\right)^{-1/2}+\frac{4E\lambda}{i\omega(2\lambda r+3)}\right]e^{i\omega T(r)}\,. \end{aligned} \tag{3.64}$$

Here m_0 is the rest mass, v_0 is the speed of the particle at spatial infinity, and $E = m_0/\sqrt{1-v_0^2}$ is the (conserved) energy per unit mass of the infalling particle. For a particle falling from rest at infinity, $E = 1$; for a particle falling ultrarelativistically, $E \to \infty$.

Since we work in perturbation theory, the amplitude of the radiation is proportional to $m_0 E$, and therefore it is useful to define the following rescaled quantities:

$$\widetilde{C}_q = \frac{C_q^{(+)}}{m_0 E}\,, \quad \widetilde{I}_q = \frac{I_q^{(+)}}{m_0 E}\,. \tag{3.65}$$

The function $T(r)$ can be found by integrating the geodesic equations, namely

$$\frac{dT}{dr} = \frac{-rE}{(r-1)\sqrt{E^2-1+1/r}}\,. \tag{3.66}$$

In order to compute the time-domain waveform generated by an infalling particle, we first work in the frequency domain. For a fixed (real) frequency ω, we integrate the homogeneous Zerilli equation using a fourth-order accurate Runge-Kutta integrator. We use the boundary condition that $\Psi^{(+)} \sim e^{-i\omega r_*}$ close to the horizon and we integrate the homogeneous equation outwards up to some large value of r. Starting from the numerically constructed homogeneous solutions, we can use a Green's function technique to find the solution of the inhomogeneous equation [72, 71, 19]. Finally, we perform an inverse Fourier transform to compute the time-domain wave function.

$E=1$	$l=2$	$l=3$	$l=4$	$l=5$
$n=0$	-1.89425 $-0.906608\,\mathrm{i}$	-0.184934 $-0.231572\,\mathrm{i}$	-0.0178934 $-0.0566232\,\mathrm{i}$	0.000637468 $-0.0141310\,\mathrm{i}$
$n=1$	-1.94463 $-0.521963\,\mathrm{i}$	-0.226114 $-0.187532\,\mathrm{i}$	-0.0288733 $-0.0511510\,\mathrm{i}$	-0.00228156 $-0.0137320\,\mathrm{i}$
$n=2$	-2.02880 $-0.263614\,\mathrm{i}$	-0.266489 $-0.148876\,\mathrm{i}$	-0.0393956 $-0.0457755\,\mathrm{i}$	-0.00509258 $-0.0132048\,\mathrm{i}$
$n=3$	-2.11182 $-0.115656\,\mathrm{i}$	-0.306561 $-0.116049\,\mathrm{i}$	-0.0496969 $-0.0405565\,\mathrm{i}$	-0.00784699 $-0.0125698\,\mathrm{i}$
$E=10$	$l=2$	$l=3$	$l=4$	$l=5$
$n=0$	-4.835573 $+0.874861\,\mathrm{i}$	-1.195880 $+0.0709923\,\mathrm{i}$	-0.449316 $+0.0101960\,\mathrm{i}$	-0.209552 $+0.00308825\,\mathrm{i}$
$n=1$	-4.478522 $+0.683019\,\mathrm{i}$	-1.177329 $+0.0667378\,\mathrm{i}$	-0.446281 $+0.0112097\,\mathrm{i}$	-0.208268 $+0.00284264\,\mathrm{i}$
$n=2$	-4.142391 $+0.502502\,\mathrm{i}$	-1.156297 $+0.0606733\,\mathrm{i}$	-0.443514 $+0.0110150\,\mathrm{i}$	-0.207551 $+0.00277215\,\mathrm{i}$
$n=3$	-3.818084 $+0.354501\,\mathrm{i}$	-1.134168 $+0.0540593\,\mathrm{i}$	-0.440663 $+0.0104592\,\mathrm{i}$	-0.206954 $+0.00269149\,\mathrm{i}$

Table 3.3

Rescaled integrals $\widetilde{I}_q$ for $l = 2$, 3, 4, 5 for particle with energy $E = 1$ (top) and $E = 10$ (bottom).

3.2.3 Regularization at the horizon

In order to find the excitation factors, one needs to evaluate Eq. (3.62) at the complex QNM frequency. At the horizon ($r \to 1$) the integrand appearing in the quantity $I_q^{(+)}$, as defined in Eq. (3.63), can be written as a Frobenius series of the form

$$e^{i\omega_q r_*}\psi_q^{(+)}(r)q^{(+)}(r,\omega_q) = \sum_{n=0}^{\infty}\xi_n(r-1)^{\zeta_q+n}\,. \tag{3.67}$$

The convergent or divergent nature of the integral depends on the value of ζ_q, which in turn is determined by the behavior of the source term $q(r,\omega_q)$ as $r \to 1$. Since the wave function $\psi_q^{(+)}(r) \sim (r-1)^{-2i\omega_q}$ as $r \to 1$, the source term (3.64) diverges as $(r-1)^{1-i\omega_q}$ at the horizon. Therefore $\zeta_q = -2i\omega_q$ and the integral is, in general, divergent. The divergence can be regularized following the method proposed by Detweiler and Szedenits [57]. The idea

$E=1$	$l=2$	$l=3$	$l=4$	$l=5$
$n=0$	-0.164989 $-0.243495\,\mathrm{i}$	0.00228872 $+0.0319187\,\mathrm{i}$	0.00280101 $-0.00475425\,\mathrm{i}$	-0.00108031 $+0.000466722\,\mathrm{i}$
$n=1$	-0.440736 $+0.409836\,\mathrm{i}$	0.0930598 $-0.0238868\,\mathrm{i}$	-0.0204455 $-0.00732461\,\mathrm{i}$	0.00323146 $+0.00470595\,\mathrm{i}$
$n=2$	0.587721 $+0.223120\,\mathrm{i}$	-0.0859447 $-0.119540\,\mathrm{i}$	-0.000483324 $+0.0436992\,\mathrm{i}$	0.00865255 $-0.0111907\,\mathrm{i}$
$n=3$	-0.216793 $-0.444266\,\mathrm{i}$	-0.0549996 $+0.146142\,\mathrm{i}$	0.0534710 $-0.0275273\,\mathrm{i}$	-0.0232746 $-0.00536977\,\mathrm{i}$
$E=10$	$l=2$	$l=3$	$l=4$	$l=5$
$n=0$	-0.646559 $-0.235935\,\mathrm{i}$	0.110752 $+0.0668420\,\mathrm{i}$	-0.0286191 $-0.0304143\,\mathrm{i}$	0.00785932 $+0.0155636\,\mathrm{i}$
$n=1$	-0.537460 $+1.242920\,\mathrm{i}$	0.208289 $-0.324589\,\mathrm{i}$	-0.122114 $+0.111058\,\mathrm{i}$	0.0768867 $-0.0372097\,\mathrm{i}$
$n=2$	1.27404 $+0.144452\,\mathrm{i}$	-0.517466 $-0.210031\,\mathrm{i}$	0.246188 $+0.206043\,\mathrm{i}$	-0.109831 $-0.176008\,\mathrm{i}$
$n=3$	-0.507006 $-0.739057\,\mathrm{i}$	0.0267961 $+0.540228\,\mathrm{i}$	0.156039 $-0.382678\,\mathrm{i}$	-0.232685 $+0.239092\,\mathrm{i}$

Table 3.4

Rescaled excitation coefficients $\widetilde{C}_q$ for $l = 2$, 3, 4, 5 for particle with energy $E = 1$ (top) and $E = 10$ (bottom).

is to add to the integrand a total derivative which vanishes at the horizon:

$$f(r) \equiv \frac{d}{dr}\left(\sum_{n=0}^{N} b_n \frac{(r-1)^{\zeta_q+n+1}}{\zeta_q+n+1} e^{-(r-1)}\right) , \tag{3.68}$$

where N is greater than (or equal to) the largest integer in the real part of $-2i\omega_q$. For Schwarzschild infalls, the coefficients b_n in this expansion can be determined order-by-order in terms of the ξ_n. The first few coefficients are listed in Appendix 1.1, and the values of the "excitation integrals" $\widetilde{I}_q$ are listed in Table 3.3.

The values of the corresponding excitation coefficients $\widetilde{C}_q = B_q^{(+)}\widetilde{I}_q$ are listed in Table 3.4. These tables were produced using a constant value $N = 2$ in Eq. (3.68), which is sufficient to regularize the divergence for the first few overtones ($n = 0\,, 1\,, 2\,, 3$). We verified that our results are insensitive to variations of N within at least six digits, as long as N is

large enough to eliminate the divergence.

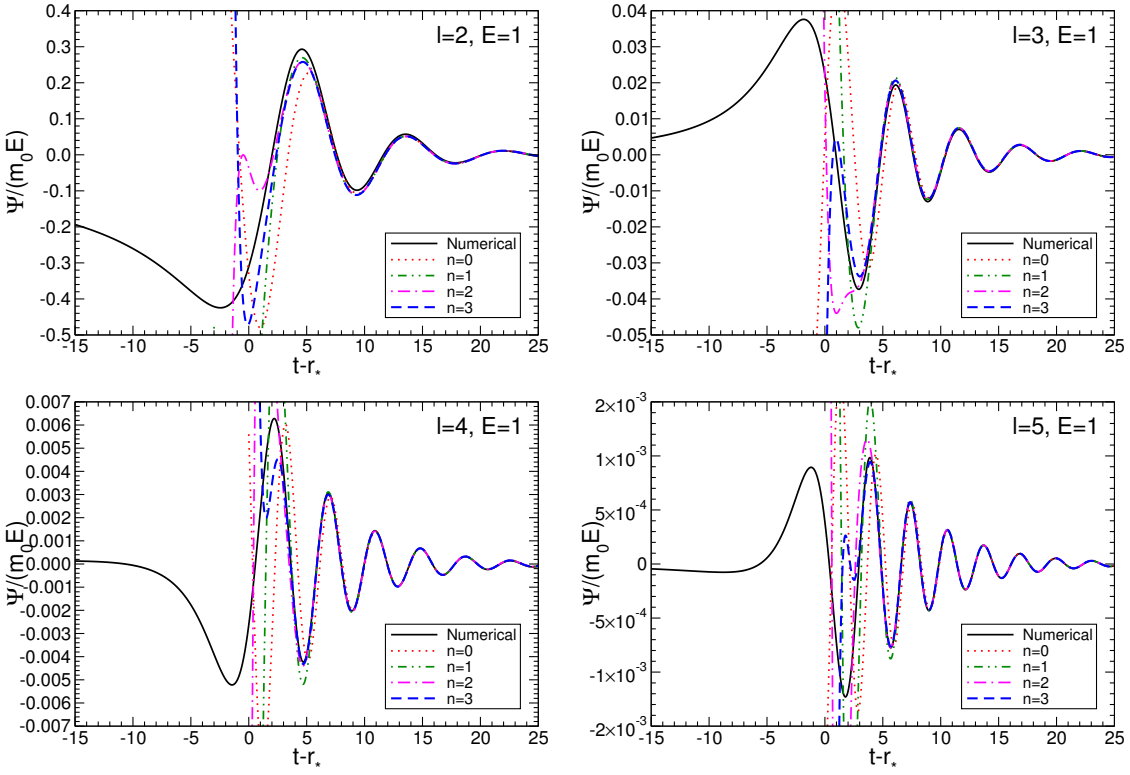

Figure 3.1

Different multipolar components of the radiation ($l = 2, 3, 4, 5$) for an infall from rest. Solid black lines are obtained from a numerical solution of the perturbation equations in the Fourier domain [19, 68], followed by an inverse Fourier transform. The other lines are obtained by summing an increasing numbers of overtones in the excitation coefficient calculation, as indicated in the legend. In this plot, as everywhere else in the paper, we use units $2M = 1$.

The tables show some interesting trends. For example, if we consider infalls from rest ($E = 1$) and a fixed multipolar index l, we see that the real part of the excitation integral $\widetilde{I}_q$ increases as a function of the overtone index n. However this increase is compensated by a comparable decrease in the imaginary part of $\widetilde{I}_q$, so that $|\widetilde{I}_q|$ is roughly constant as a function of n.

Figure 3.1 compares the excitation coefficient calculation of Eq. (3.8) against numerical gravitational waveforms for particles falling radially from rest. These waveforms were

computed using the frequency-domain codes described in Refs. [19, 68], and then Fourier-transformed back in time. Each panel corresponds to a fixed multipole index ($l = 2\,, 3\,, 4\,, 5$), and different line styles correspond to ringdown waveforms obtained summing a different number of overtones. This plot generalizes and extends a similar comparison that can be found in Fig. 10 of Leaver's original paper [25]. Leaver found a disagreement at the 10% level, that he attributed to inaccuracies in the Fourier transform of the numerical waveforms. We have similar accuracy problems with the Fourier transform of our data (computing Fourier amplitudes at low frequencies ω is time consuming, because the computational domain must extend out to a radius $r \sim 1/\omega$), but the level of disagreement that we observe is smaller than in Leaver's original analysis. Furthermore, the agreement between our numerics and the excitation coefficient calculation gets better as l grows. Figure 3.1 shows quite clearly that the addition of higher overtones generally improves the agreement between the excitation coefficient calculation and the full numerical waveform at early times. However there is no analytical proof that the expansion in terms of overtones should be convergent [25], and indeed in a few isolated cases an expansion including a large number of overtones can perform more poorly than a similar expansion including a smaller number of overtones.

Figure 3.2 is similar to Figure 3.1, but it refers to a relativistic infall with (normalized) particle energy $E = 10$. This figure shows that even by adding four overtones we don't get excellent agreement at the "absolute maximum" of the numerical waveform. Part of the reason is that we can only get accurate numerical amplitudes at frequencies $M\omega \gtrsim 10^{-3}$: to remove "memory effects" in the inverse Fourier transform, we extrapolate our numerical calculations to obtain the Fourier-domain waveform amplitude at frequencies $M\omega \lesssim 10^{-3}$. More importantly, in ultrarelativistic infalls a larger fraction of the energy is radiated during the infall (at low frequencies) than in the case of infalls from rest. In other words, a larger fraction of the radiation is produced *before* the beginning of the ringdown phase, and this explains the larger disagreement between numerical waveforms and "pure ringdown" waveforms. As in the nonrelativistic case, we observe that: (i) the ringdown waveform agrees

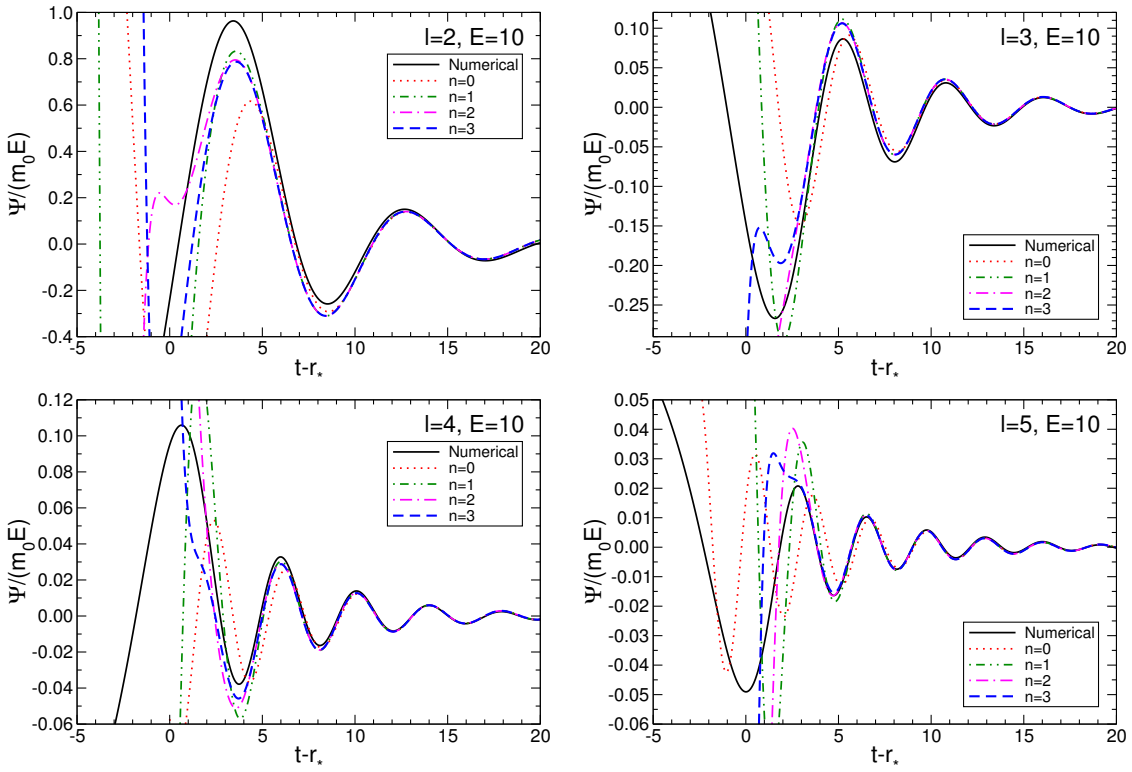

Figure 3.2

Different multipolar components of the radiation ($l = 2, 3, 4, 5$) for an infall with initial energy $E = 10$. Solid black lines are results from the numerical solution of the perturbation equations; the other lines are results obtained by summing different numbers of overtones. In this plot, as everywhere else in the paper, we use units $2M = 1$.

better with the numerical solution as l grows; (ii) the addition of higher overtones improves the agreement between the excitation coefficient expansion and the numerical waveforms, but to a lesser extent, for the reasons explained above.

3.3 Excitation factors and excitation coefficients for Kerr black holes

In this section we extend our calculation to particles falling into Kerr BHs. For simplicity, we consider a particle falling ultrarelativistically along the symmetry axis. In this case the source term of the Sasaki-Nakamura equation (3.41) simplifies considerably [72, 71]:

$$\mathcal{S} = -\frac{m_0 E C_l^a \gamma \Delta}{2\omega^2 r^2 (r^2+a^2)^{3/2}} e^{-i\omega r_*}\,, \tag{3.69}$$

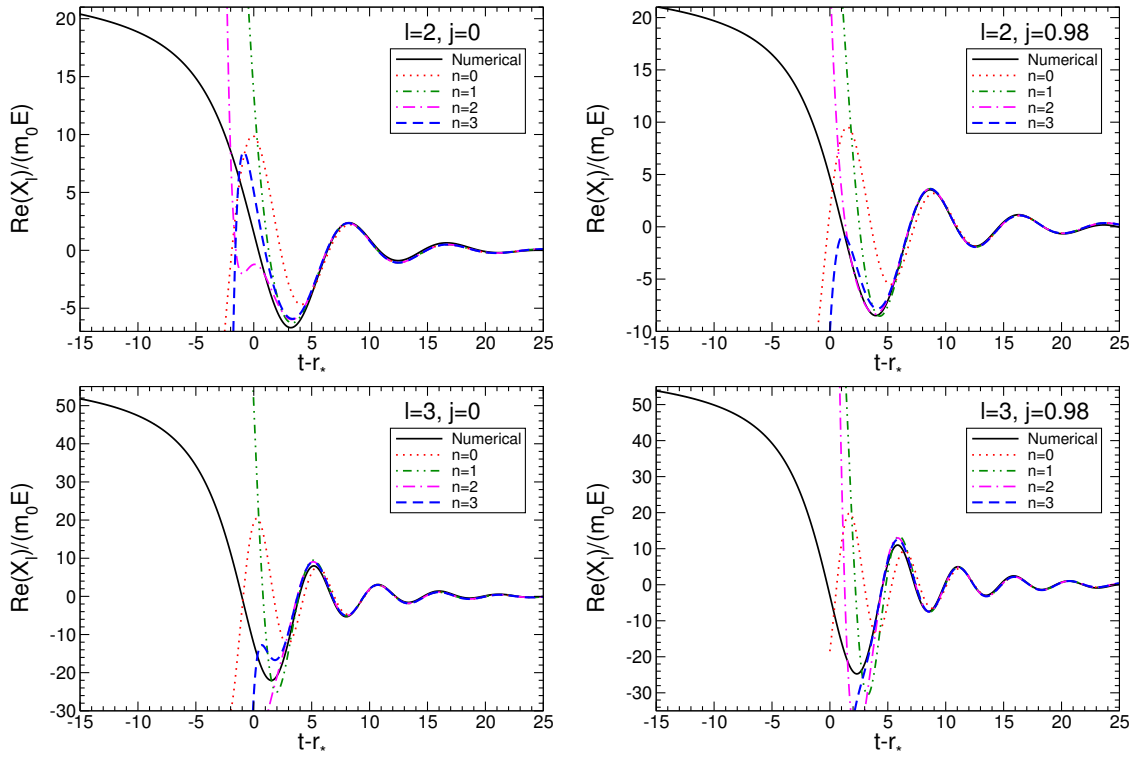

Figure 3.3

Sasaki-Nakamura wave function for an ultrarelativistic infall along the symmetry axis of a Kerr BH. Solid black lines are results from the numerical solution of the perturbation equations; the other lines are results obtained by summing different numbers of overtones. The upper panels refer to $l = 2$, the lower panels to $l = 3$. The left panels corresponds to the Schwarzschild limit ($j = 0$), and the right panels to a fast-spinning Kerr BH with $a = 0.49$ ($j = 0.98$). In this plot, as everywhere else in the paper, we use units $2M = 1$.

where

$$C_l^a = \lim_{\theta\to 0} \frac{8 S_{l0\omega}(\theta,\phi)}{\sin^2\theta}\,, \tag{3.70}$$

and γ was defined in (3.43). The constants C_l^a were determined by solving the angular eigenvalue problem through a continued fraction representation, and then plugging these eigenvalues into the series solution providing the spheroidal wave functions $S_{l0\omega}$ [16, 12]. The procedure to determine the time-domain solution of the Sasaki-Nakamura wave function X is identical to that adopted for the Schwarzschild case: i.e., first we solve the equations in the frequency domain, and then we Fourier transform back in time, applying a low-frequency

extrapolation when this is necessary to remove memory effects.

Figure 3.3 (which is similar to Figure 3.1) compares the excitation coefficient calculation of Eq. (3.8) – where now Ψ must be understood as the Sasaki-Nakamura wave function – against numerical gravitational waveforms obtained in this way. As in the Schwarzschild case, the integrand appearing in the calculation of the Kerr excitation factors is, in general, divergent. The divergence can be regularized following a procedure analogous to the Schwarzschild case (cf. Appendix 1.2).

Figure 3.3 confirms our basic findings from the nonrotating case: the convergence of the QNM expansion is not necessarily monotonic, and the excitation coefficient expansion works better for higher values of l. Notice that a relatively small number of overtones is sufficient to reproduce the numerical waveform at early times even when the spin of the Kerr BH is rather large ($j = 0.98$), so that one may in principle expect that a larger number of overtones would be necessary (see, e.g., Refs. [46, 69, 14, 15, 39]). To our knowledge, the calculation presented in this Section is the first concrete proof that an excitation-coefficient expansion is applicable and useful in the Kerr case: all calculations available in the literature so far were specific to the Schwarzschild case (see, e.g., Refs. [55, 56]).

CHAPTER 4

CONCLUSIONS

In chapter 2, we extended the method proposed in Ref. [50] to determine the formal region of validity of the PN approximation for quasicircular EMRIs of compact objects in the equatorial plane of a Kerr BH. The boundary of the formal region of validity is defined as the orbital velocity where the "true" error in the approximation (relative to high-accuracy numerical calculations) becomes comparable to the series truncation error (due to neglecting higher-order terms in the series).

For quasicircular, equatorial Kerr EMRIs, the PN expansion is known up to 4PN, and our estimate of the region of validity can only be pushed up to 3PN. Our main results are shown in Fig. 2.4 (in terms of orbital velocity) and in Fig. 2.5 (in terms of orbital radius). At fixed but arbitrary spin parameter a, the 3PN approximation has no obvious advantage when compared with other PN orders. At fixed PN order N, Fig. 2.4 shows an interesting trend: when normalized by the ISCO velocity $v_{\rm ISCO}$, to a very good approximation the region of validity does not depend on a.

We should emphasize that our results say nothing about the absolute accuracy of the PN approximation: they only suggest relational statements between the Nth and the $(N+1)$th-order approximations. For velocities within the region of validity of the asymptotic series, all we can say is that the Nth order approximation has errors that are of expected relative size. For larger velocities, the $(N+1)$th- and higher-order terms become important, and should not be formally neglected. If we can tolerate errors larger than those estimated by the $(N+1)$th order term (at the risk that higher-order approximations may be less accurate than lower-order ones) we can surely use the PN expansion beyond the realm of its formal

region of validity. This, however, would force us to lose analytic control of the magnitude of the error, as given by the next order term. The meaning of this caveat is well illustrated by the counterrotating case with $a = -0.99$: it is clear from Fig. 2.2 that the 3.5PN and 4PN approximations do *not* represent an improvement over the 3PN approximation (and in fact perform quite badly) beyond the realm of the region of validity.

In chapter 3, we have implemented a new method, based on the MST formalism, to compute the excitation factors B_q for Kerr QNMs. This method is simpler and more accurate than the method used by Berti and Cardoso in Ref. [9], allowing us to extend the calculation to higher angular multipoles l and to higher overtone numbers n. Tables of the excitation factors B_q in the Teukolsky and Sasaki-Nakamura formalisms were made publicly available online [76], in the hope to stimulate further research in this field.

As a test of the method, we computed the QNM excitation coefficients for the classic problem of particles falling radially into the BH. We have compared the excitation coefficient expansion against numerical results for: (i) particles falling from rest ($E = 1$) into a Schwarzschild BH, (ii) large-energy particles ($E = 10$) falling into a Schwarzschild BH, and (iii) ultrarelativistic particles falling into a Kerr BH along the symmetry axis. In all cases we found excellent agreement, validating the usefulness of excitation coefficient calculations in the analytical modeling of the ringdown phase.

BIBLIOGRAPHY

BIBLIOGRAPHY

[1] A. H. Mroue, L. E. Kidder, S. A. Teukolsky (2008), Phys. Rev. **D78**, 044004 (2008). [arXiv:0805.2390 [gr-qc]].

[2] A. Taracchini, Y. Pan, A. Buonanno, E. Barausse, M. Boyle, *et al.* (2012), Phys. Rev. **D86**, 024011 (2012), arXiv:1202.0790 [gr-qc] .

[3] Bender, C. M. and Orszag, S. A. (1978), *Advanced Mathematical Methods for Scientists and Engineers,* New York: McGraw-Hill, 1978.

[4] C. O. Lousto and R. H. Price (1997), Phys. Rev. **D55**, 2124 (1997), arXiv:gr-qc/9609012.

[5] C. O. Lousto, H. Nakano, Y. Zlochower, and M. Campanelli (2010), Phys. Rev. **D82**, 104057 (2010), arXiv:1008.4360 [gr-qc] .

[6] C. O. Lousto, H. Nakano, Y. Zlochower, B. C. Mundim, and M. Campanelli (2012), Phys. Rev. **D85**, 124013 (2012), arXiv:1203.3223 [gr-qc] .

[7] D. Pollney, C. Reisswig (2010), arXiv:1004.4209 [gr-qc].

[8] D. Pollney, C. Reisswig, E. Schnetter, N. Dorband, P. Diener (2011), Phys. Rev. **D83**, 044045 (2011). [arXiv:0910.3803 [gr-qc]].

[9] E. Berti and V. Cardoso (2006), Phys. Rev. **D74**, 104020 (2006), arXiv:gr-qc/0605118.

[10] E. Berti, M. Cavaglia, and L. Gualtieri (2004), Phys. Rev. **D69**, 124011 (2004), arXiv:hep-th/0309203 .

[11] E. Berti, M. Volonteri (2008), Astrophys. J. **684**, 822-828 (2008). [arXiv:0802.0025 [astro-ph]].

[12] E. Berti, V. Cardoso, and A. O. Starinets (2009), Class. Quantum Grav. 26, 163001 (2009), arXiv:0905.2975 [gr-qc].

[13] E. Berti, V. Cardoso, and B. Kipapa (2011), Phys. Rev. **D83**, 084018 (2011), arXiv:1010.3874 [gr-qc] .

[14] E. Berti, V. Cardoso, and C. M. Will (2006), Phys. Rev. **D73**, 064030 (2006c), arXiv:grqc/0512160 .

[15] E. Berti, V. Cardoso, and C. M. Will (2006), AIP Conf. Proc. 848, 687 (2006b), arXiv:gr-qc/0601077 .

[16] E. Berti, V. Cardoso, and M. Casals (2006), Phys. Rev. **D73**, 024013 (2006a), arXiv:grqc/0511111 .

[17] E. Berti, V. Cardoso, J. A. Gonzalez, U. Sperhake, B. Bruegmann (2008), Class. Quant. Grav. **25**, 114035 (2008). [arXiv:0711.1097 [gr-qc]].

[18] E. Berti, V. Cardoso, J. A. Gonzalez, U. Sperhake, M. Hannam, S. Husa, B. Bruegmann (2007), Phys. Rev. **D76**, 064034 (2007). [gr-qc/0703053 [GR-QC]].

[19] E. Berti, V. Cardoso, T. Hinderer, M. Lemos, F. Pretorius, U. Sperhake, and N. Yunes (2010), Phys. Rev. **D81**, 104048 (2010), arXiv:1003.0812 [gr-qc] .

[20] E. K. Porter (2007), Phys. Rev. **D76**, 104002 (2007). [arXiv:0706.0114 [gr-qc]].

[21] E. Mitsou (2011), Phys. Rev. **D83**, 044039 (2011), arXiv:1012.2028 [gr-qc] .

[22] E. N. Dorband, E. Berti, P. Diener, E. Schnetter, and M. Tiglio (2006), Phys. Rev. **D74**, 084028 (2006), arXiv:gr-qc/0608091 .

[23] E. Poisson (1995), Phys. Rev. **D52**, 5719-5723 (1995). [gr-qc/9505030].

[24] E. W. Leaver (1985), Proc. R. Soc. London, Ser. A 402, 285 (1985).

[25] E. W. Leaver (1986), Phys. Rev. **D34**, 384 (1986).

[26] F. J. Zerilli (1970), Phys. Rev. **D2**, 2141 (1970).

[27] F. Pretorius (2007), "Binary Black Hole Coalescence," in Physics of relativistic objects in compact binaries: from birth to coalescence (Astrophysics and Space Science Library, Vol. 359) (Springer, New York, 2007) Chap. 9, arXiv:0710.1338 [gr-qc].

[28] G. Lovelace, M. Boyle, M. A. Scheel, and B. Szilagyi (2012), Class. Quantum Grav. 29, 045003 (2012), arXiv:1110.2229 [gr-qc] .

[29] G. Lovelace, M. Scheel, and B. Szilagyi (2011), Phys. Rev. **D83**, 024010 (2011), arXiv:1010.2777 [gr-qc] .

[30] G. Lovelace, R. Owen, H. P. Pfeiffer, and T. Chu (2008), Phys. Rev. **D78**, 084017 (2008), arXiv:0805.4192 [gr-qc] .

[31] H. Kodama and A. Ishibashi (2003), Prog. Theor. Phys. 110, 701 (2003), arXiv:hepth/0305147 .

[32] H. M. S. Yoshino and M. Shibata (2011), Prog.Theor.Phys.Suppl. 189, 269 (2011).

[33] H. Nakano, Y. Zlochower, C. O. Lousto, and M. Campanelli (2011), Phys. Rev. **D84**, 124006 (2011), arXiv:1108.4421 [gr-qc] .

[34] H. P. Nollert (1999), Class. Quantum Grav. 16, R159 (1999).

[35] H. P. Nollert and R. H. Price (1999), J. Math. Phys. 40, 980 (1999), arXiv:gr-qc/9810074.

[36] H. P. Pfeiffer (2012), Class. Quant. Grav. 29, 124004 (2012), arXiv:1203.5166 [gr-qc].

[37] H. Tagoshi, M. Shibata, T. Tanaka, M. Sasaki (1996), Phys. Rev. **D54**, 1439-1459 (1996). [gr-qc/9603028].

[38] H. Witek, V. Cardoso, L. Gualtieri, C. Herdeiro, U. Sperhake, and M. Zilhao (2011), Phys. Rev. **D83**, 044017 (2011), arXiv:1011.0742 [gr-qc] .

[39] H. Yang, F. Zhang, A. Zimmerman, D. A. Nichols, E. Berti, *et al.* (2013), Phys. Rev. **D87**, 041502 (2013), arXiv:1212.3271 [gr-qc] .

[40] J. A. Gonzalez, U. Sperhake, and B. Brugmann (2009), Phys. Rev. **D79**, 124006 (2009), arXiv:0811.3952 [gr-qc].

[41] J. M. Bardeen, W. H. Press, S. A. Teukolsky (1972), Astrophys. J. **178**, 347 (1972).

[42] K. D. Kokkotas and B. G. Schmidt (1999), Living Rev. Relativity 2 (1999), arXiv:grqc/9909058.

[43] M. Davis, R. J. Ruffini, W. H. Press, and R. H. Price (1971), Phys. Rev. Lett. 27, 1466 (1971).

[44] M. Sasaki and H. Tagoshi (2003), Living Rev. Relativity 6 (2003), arXiv:gr-qc/0306120.

[45] M. Sasaki and T. Nakamura (1982), Prog. Theor. Phys. 67, 1788 (1982).

[46] N. Andersson and K. Glampedakis (2000), Phys. Rev. Lett. 84, 4537 (2000), arXiv:grqc/9909050 [gr-qc] .

[47] N. Yunes (2009), GW Notes, Vol. 2, p. 3-47 (2009).

[48] N. Yunes, A. Buonanno, S. A. Hughes, M. Coleman Miller, Y. Pan (2010), Phys. Rev. Lett. **104**, 091102 (2010). [arXiv:0909.4263 [gr-qc]].

[49] N. Yunes, A. Buonanno, S. A. Hughes, Y. Pan, E. Barausse, M. C. Miller, W. Throwe (2011), Phys. Rev. **D83**, 044044 (2011). [arXiv:1009.6013 [gr-qc]].

[50] N. Yunes, E. Berti. (2008), Phys. Rev. **D77**, 124006 (2008). [arXiv:0803.1853 [gr-qc]].

[51] S. A. Teukolsky (1972), Phys. Rev. Lett. 29, 1114 (1972).

[52] S. A. Teukolsky (1973), Astrophys. J. 185, 635 (1973).

[53] S. Bernuzzi, A. Nagar, A. Zenginoglu (2011), Phys. Rev. **D83**, 064010 (2011). [arXiv:1012.2456 [gr-qc]].

[54] S. Chandrasekhar (1983), *The Mathematical Theory of Black Holes* (Clarendon Press, Oxford, U.K., 1983).

[55] S. Hadar and B. Kol (2011), Phys. Rev. **D84**, 044019 (2011), arXiv:0911.3899 [gr-qc] .

[56] S. Hadar, B. Kol, E. Berti, and V. Cardoso (2011), Phys. Rev. **D84**, 047501 (2011), arXiv:1105.3861 [gr-qc] .

[57] S. L. Detweiler and J. Szedenits, Eugene (1979), Astrophys. J. 231, 211 (1979).

[58] S. Mano and E. Takasugi (1997), Prog. Theor. Phys. 97, 213 (1997), arXiv:grqc/9611014 .

[59] S. Mano, H. Suzuki, and E. Takasugi (1996), Prog. Theor. Phys. 96, 549 (1996b), arXiv:gr-qc/9605057 .

[60] S. Mano, H. Suzuki, and E. Takasugi (1996), Prog. Theor. Phys. 95, 1079 (1996a), arXiv:gr-qc/9603020 .

[61] T. Damour, B. R. Iyer, A. Nagar (2009), Phys. Rev. **D79**, 064004 (2009). [arXiv:0811.2069 [gr-qc]].

[62] T. Damour, B. R. Iyer, B. S. Sathyaprakash (1998), Phys. Rev. **D57**, 885-907 (1998). [gr-qc/9708034].

[63] T. Damour, B. R. Iyer, B. S. Sathyaprakash (2001), Phys. Rev. **D63**, 044023 (2001). [gr-qc/0010009].

[64] T. Regge and J. A. Wheeler (1957), Phys. Rev. 108, 1063 (1957).

[65] T. Tanaka, H. Tagoshi, M. Sasaki (1996), Prog. Theor. Phys. **96**, 1087-1101 (1996). [gr-qc/9701050].

[66] U. Sperhake (2013), arXiv:1301.3772 [gr-qc].

[67] U. Sperhake, E. Berti, and V. Cardoso (2011), arXiv:1107.2819 [gr-qc].

[68] U. Sperhake, V. Cardoso, C. D. Ott, E. Schnetter, and H. Witek (2011), Phys. Rev. **D84**, 084038 (2011b), arXiv:1105.5391 [gr-qc] .

[69] V. Cardoso (2004), Phys. Rev. **D70**, 127502 (2004), arXiv:gr-qc/0411048 .

[70] V. Cardoso and J. P. S. Lemos (2002), Phys. Lett. **B538**, 1 (2002), arXiv:gr-qc/0202019.

[71] V. Cardoso and J. P. S. Lemos (2003), Phys. Rev. **D67**, 084005 (2003b), arXiv:grqc/0211094 .

[72] V. Cardoso and J. P. S. Lemos (2003), Gen. Rel. Grav. 35, 327 (2003a), arXiv:grqc/0207009 .

[73] V. Cardoso, L. Gualtieri, C. Herdeiro, U. Sperhake, P. M. Chesler, *et al.* (2012), Class. Quant. Grav. 29, 244001 (2012), arXiv:1201.5118 [hep-th] .

[74] V. Ferrari and R. Ruffini (1981), Phys. Lett. **B98**, 381 (1981).

[75] W. E. East and F. Pretorius (2013), arXiv:1303.1540 [gr-qc] .

[76] Webpage (2013), Webpage with Mathematica notebooks and numerical quasinormal mode Tables: http://www.phy.olemiss.edu/ berti/qnms.html http://gamow.ist.utl.pt/ vitor/ringdown.html .

[77] Y. Mino, M. Sasaki, M. Shibata, H. Tagoshi, T. Tanaka (1997), Prog. Theor. Phys. Suppl. **128**, 1-121 (1997). [gr-qc/9712057].

[78] Y. Pan, A. Buonanno, R. Fujita, E. Racine, H. Tagoshi (2011), Phys. Rev. **D83**, 064003 (2011). [arXiv:1006.0431 [gr-qc]].

[79] Y. Sun and R. H. Price (1988), Phys. Rev. **D38**, 1040 (1988).

APPENDIX

APPENDIX

1 Regularization coefficients

1.1 The Schwarzschild case

For reference, in this Appendix we list the first few regularization coefficients b_n defined in Eq. (3.68):

$$
\begin{aligned}
b_0 &= \xi_0\,, \qquad (.1)\\
b_1 &= \xi_1 + \frac{2-2i\omega_q}{1-2i\omega_q}\, b_0\,,\\
b_2 &= \xi_2 + \frac{2i\omega_q-3}{2(1-2i\omega_q)}\, b_0 + \frac{3-2i\omega_q}{2(1-i\omega_q)}\, b_1\,,\\
b_3 &= \xi_3 + \frac{2-i\omega_q}{3(1-2i\omega_q)}\, b_0 + \frac{i\omega_q-2}{2(1-i\omega_q)}\, b_1 + \frac{2(2-i\omega_q)}{3-2i\omega_q}\, b_2\,,\\
b_4 &= \xi_4 + \frac{2i\omega_q-5}{24(1-2i\omega_q)}\, b_0 + \frac{5-2i\omega_q}{12(1-i\omega_q)}\, b_1\\
&+ \frac{2i\omega_q-5}{2(3-2i\omega_q)}\, b_2 + \frac{5-2i\omega_q}{2(2-i\omega_q)}\, b_3\,.
\end{aligned}
$$

1.2 The Kerr case

The regularization coefficients for the Kerr case are much more lengthy than in the nonrotating case, but their calculation is straightforward. Here we list for reference the first

two coefficients:

$$
\begin{aligned}
b_0 &= \frac{1}{A_{\rm out}\ \omega_q^2 r_+^2}(r_+ - r_-)^{\left(\frac{2i\omega_q r_+}{r_+ - r_-}-1\right)}(ir_+ - ir_- + \omega_q\, r_+)(2ir_+ - i + 2\omega_q r_+)\,, \qquad (.2)\\
b_1 &= 2b_0\frac{r_- - r_+ + i\omega_q r_+}{r_- - r_+ + 2i\omega_q r_+} + \frac{1}{2A_{\rm out}^{\rm SN}\omega_q^2}\frac{1}{r_+^3}(r_+ - r_-)^{\frac{3r_+ - 3r_- - 2i\omega_q r_+}{r_- - r_+}}\\
&\times \left\{ r_-^4(8 + 4ir_+\omega_q) + r_-^3\Big[4 + r_+(-36 + \lambda + 12i\omega_q) - 2r_+^2\omega_q(5i + 2\omega_q)\Big]\right.\\
&+ r_-^2 r_+\Big[4i\omega_q - 11 + 6r_+^2\omega_q(i + 2\omega_q) + 3a_{r1}\\
&\qquad - r_+(3\lambda - 58 + 38i\omega_q + 4\omega_q^2 + 6a_{r1} - 6i\omega_q a_{r1})\Big]\\
&+ r_+^3\Big[4\omega_q^2 + 2r_+^2\omega_q(2\omega_q - i) - 2i\omega_q(a_{r1} - 5) + 3(a_{r1} - 1)\\
&\qquad - r_+\Big(\lambda + 2(1 - i\omega_q)\big(4\omega_q^2 - 5 - 2i\omega_q(a_{r1} - 4) + 3a_{r1}\big)\Big)\Big]\\
&+ r_- r_+^2\Big[2r_+^2(i - 6\omega_q)\omega_q + 2\big(5 + i\omega_q(-7 + a_{r1}) - 3a_{r1}\big)\\
&\qquad \left. + r_+\Big(3\lambda - 4\big(10 + \omega_q^2(-5 + a_{r1}) - 3a_{r1} + i\omega_q(-13 + 4a_{r1})\big)\Big)\Big]\right\},
\end{aligned}
$$

where

$$\sigma_+ = \frac{\omega_q r_+ - am}{r_+ - r_-}\,, \qquad (.3)$$

the amplitude $A_{\rm out}^{\rm SN}$ is related to the Teukolsky amplitude $A_{\rm out}^{\rm T} = \sum_{n=0}^{\infty} a_{rn}$ via Eq. (3.47) and λ is related to the separation constant A_{lm} through relation (3.20). The coefficients $\{a_{rn}\}$, $n = 0,\ 1,\ 2...$ (with $a_{r0} = 1$) are defined via the homogeneous solution R_{r_+} of the Teukolsky equation

$$R_{r_+} = e^{i\omega_q r}(r - r_-)^{-1-s+i\omega_q+i\sigma_+}(r - r_+)^{-s-i\sigma_+}\sum_{n=0}^{\infty} a_{rn}\left(\frac{r - r_+}{r - r_-}\right)^n\,, \qquad (.4)$$

and can be obtained by plugging this decomposition in the Teukolsky equation (3.10).

The Sasaki-Nakamura wave function X is related to R_{r_+} by Eq. (3.38). What we plot in Figure 3.3 is actually the normalized Sasaki-Nakamura wave form $X_q^{\rm SN} = (Xe^{-i\omega_q r_*})/A_{\rm out}$,

whose excitation coefficients are given by

$$C_q = -\gamma_\infty \int_{r_+}^{\infty} \left[\frac{X_q^{\rm SN}}{2\omega_q^2 r^2 \sqrt{(r-r_+)(r-r_-)+r}} - \sum_{k=0}^{\infty} \left(e^{-r+r_+} (r-r_+)^{k+\frac{2i\omega_q r_+}{r_- - r_+}} b_k - \frac{e^{-r+r_+} (r-r_+)^{1+k+\frac{2i\omega_q r_+}{r_- - r_+}}}{1+k+\frac{2i\omega_q r_+}{r_- - r_+}} b_k \right) \right] dr \,.$$

VITA

Contact

Name: Zhongyang Zhang

Address: Department of Physics, University of Mississippi, University, MS, 38677, U.S.A.

Email: zzy2417@gmail.com

Education

2003-2007 University of Science and Technology of China, BSc in Physics, 2007

2010-2013 The University of Mississippi, MSc in Physics, 2014

Honors & Awards

2002: First Prize in the National Mathematics Contest;

2003: Third Prize of Outstanding Student Scholarship;

2004: Third Prize in the USTC Physics Knowledge Contest;

2005: First Prize of Outstanding Student Scholarship;

2006: Guanghua Prize of Outstanding Student Scholarship;

2007: First Prize of USTC Excellent Undergraduate Thesis;

2008-2010: International Postgraduate Research Scholarships;

2010-2013: Zdravko Stipcevic Honors Fellowship.

Publications

[1] Quasinormal ringing of Kerr black holes. II. excitation by particles falling radially with arbitrary energy

Zhongyang Zhang, Emanuele Berti and Vitor Cardoso

Phys. Rev. **D88**, 044018 (2013)

http://prd.aps.org/abstract/PRD/v88/i4/e044018

[2] Accuracy of the post-Newtonian approximation. II. optimal asymptotic expansion of the energy flux for quasicircular, extreme mass-ratio inspirals into a Kerr black hole

Zhongyang Zhang, Nicolás Yunes, and Emanuele Berti

Phys. Rev. **D84**, 024029 (2011)

http://prd.aps.org/abstract/PRD/v84/i2/e024029

[3] Enhancement and suppression of opto-acoustic parametric interactions using optical feedback

Zhongyang Zhang, Chunnong Zhao, Li Ju and D.G. Blair

Phys. Rev. A 81, 013822 (2010)

http://pra.aps.org/abstract/PRA/v81/i1/e013822

[4] Quasinormal-mode spectrum of Kerr black holes and its geometric interpretation

Huan Yang, David A. Nichols, Fan Zhang, Aaron Zimmerman, Zhongyang Zhang, and Yanbei Chen

Phys. Rev. D 86, 104006 (2012)

http://prd.aps.org/abstract/PRD/v86/i10/e104006

[5] Strategies for the control of parametric instability in advanced gravitational wave detectors

L. Ju, D.G. Blair, C. Zhao, S. Gras, Z. Zhang, P. Barriga and H. Miao

Class. Quantum Grav. 26 015002 (2009)

http://iopscience.iop.org/0264-9381/26/1/015002

[6] Three-mode opto-acoustic parametric interactions with a coupled cavity

H.X. Miao and C.N. Zhao, L. Ju, S. Gras, P. Barriga, Z. Zhang and D. G. Blair

Phys. Rev. A 78, 063809 (2008)

http://pra.aps.org/abstract/PRA/v78/i6/e063809